Nano-petrophysical study of the Dean, Wolfcamp, and Canyon formations of the Midland Basin, Texas, USA.

Benton Mowrey

Presented to the Faculty of the Graduate School of

The University of Texas at Arlington in Partial Fulfillment

Of the Requirements

For the Degree of

MASTER OF SCIENCE IN PETROLEUM GEOSCIENCE

THE UNIVERSITY OF TEXAS AT ARLINGTON

DECEMBER 2019

Acknowledgements

I would like to thank Dr. Qinhong Hu for providing both exceptional mentorship and resources for my research. Dr. Hu was constantly available for consultation and guidance. It was a great pleasure to work with someone who is contributing so much to the understanding of the earth and its unconventional resources. I am very thankful for the opportunity to complete research under his guidance. I would also like to thank my committee members Dr. Loocke and Dr. Wickham for kindly volunteering their time to help guide my thesis studies.

Additionally, I would like to thank Pioneer Natural Resources and Diamondback Energy for providing core samples. Thank you to Lowelle Waite, Mriganko Sarkar, Sam Becker and Nabil Mzee for helping to procure samples. Laboratory work was made much easier with the help of Qiming Wang, Ryan Jones, and Sam Becker; thank you all!

Of course, I would like thank my parents, who have so generously contributed to my education. Thanks to my dad for taking me out with him to work, sparking an interest in geology. Finally, I'll like to extend my thanks to my grandparents, sister, and brother for their support.

ABSTRACT

The prolific levels of oil and gas production from the shale revolution have been plagued by steep initial production decline and inefficiencies in recovering the total hydrocarbons in place. Even the widespread practice of using multi-well sites with closely spaced wellbores has failed to yield a moderate fraction of the potential resources. It is hypothesized that the constraints of shale production arise from its nano-pore structure. Slow, diffuse hydrocarbon transport from the shale matrix to the stimulated fracture network is a likely production bottleneck. Understanding transport phenomena from this tight, porous matrix to the fracture via nanometer-scale pathways is essential to implementing effective recovery methods for tight shale plays. These fluid pathways are controlled by the pore size distribution, pore shape, and pore connectivity: nanometer scale properties that affect the macroscopic reservoir characteristics. This study aims to detail a variety of tests which can comprehensively characterize shale samples at the nanometer scale. Additionally, this study establishes limited pore connectivity, dual wettability, and diffuse transport as limitations on production from Dean, Wolfcamp, and Canyon formations.

Nanopetrophysical characteristics were investigated for a total of ten core samples from three wells in the Midland Basin's Dean, Wolfcamp, and Canyon formations. Pore structure and transport properties were characterized using mercury injection capillary pressure, vacuum saturation, liquid pycnometry, spontaneous imbibition, and contact angle (wettability) tests. Additionally, geochemistry and mineralogical composition were assessed with total organic carbon (TOC), pyrolysis, and X-ray powder diffraction (XRD) testing. Samples were processed in the following forms: cores, one cubic centimeter cubes, crushed sediment, and thin slabs.

Spontaneous imbibition tests for each sample exhibit significant variance in imbibition rates with fluid wettability. Imbibition slopes are in the range of the classical diffusion value of 0.5 for hydrophobic fluid, and in the anomalous diffusion range of 0.25 for hydrophobic fluid; indicative of a connected oil-wet pore-throat system and a disconnected water-wet pore-throat system. Additionally, the presence of edge-accessible and isolated porosity was probed with vacuum saturation and liquid pycnometry. Pore systems appear to be limited by the extent of connectivity of pore space to the sample edge. The presence of edge-accessible pore space is important to shale because of very low permeability (nano-darcy to milli-darcy scale). Fluid flow through the pore system to hydraulically induced fractures may be limited by pore systems which are not accessible to the fracture edge. Mercury injection capillary pressure tests show a significant volume for Wolfcamp and Canyon samples that are dominated by large pore-throats (>100 μm), possibly associated with sheet-like pore space between laminae. Dean samples show more evenly-distributed pore-throats than the Wolfcamp and Canyon samples, dominantly between 0.01-1 μm.

Contents

List of Figures

List of Tables

List of Equations

INTRODUCTION

Shale gas and tight oil production from stimulated fine-grained hydrocarbon reservoirs have been changing the energy landscape of the world. Horizontal drilling coupled with multi-stage hydraulic fracturing allows production of these source rocks. Oil production in the United States is led by the Permian Basin region – which nearly triples the daily crude oil production of the Bakken, the second highest onshore region for crude oil production (EIA, 2019). However, tight oil production in the Permian Basin, and shale plays in general, are plagued by steep decline curves. Shale rocks have inherently low permeability and require fracture stimulation to produce. It is imperative to understand the flow path from the unfractured, shale matrix to the induced fracture in order to maximize recovery of these resources. The goal of this research is to quantify various key parameters of shale core samples to assess the intertwined nature of connectivity, wettability, and structure of fine-grained pore systems.

Key geological characteristics for shale plays include: Total organic carbon (TOC), thermal maturity, mineralogical composition, organic matter type, thickness, porosity and permeability. Laboratory tests were performed to assess these parameters of shale, including the approaches of vacuum saturation, liquid pycnometry, mercury injection capillary pressure (MICP), x-ray diffraction (XRD), fluid imbibition, pyrolysis, total organic carbon, and contact angle. For vacuum saturation, liquid pycnometry, fluid imbibition, and contact angle, laboratory tests which investigate the pore structure and/or connectivity of pore systems, three fluids of different wettability characteristics are utilized: deionized water (DIW), tetrahydrofuran (THF), and a 2:1 mixture of n-decane and toluene (DT2). The response to each different fluid type should yield insight into the effect of wettability in the pore systems of the samples.

Core samples were taken from three different wells in the Midland Basin from both Pioneer Resources and Diamondback Energy. Samples were taken from the Dean, Wolfcamp, and Canyon formations.

GEOLOGICAL CONTEXT

The Permian Basin is a sedimentary system located in the foreland of the Marathon-Ouachita orogenic belt. The basin extends across 52 counties of West Texas and Southeast New Mexico. It is divided into three main sub-divisions: the Delaware Basin, Midland Basin, and Central Basin Platform. The Central Basin Platform separates the eastern Midland Basin from the western Midland Basin. The Permian Basin was deposited over the ancestral Tobosa Basin.

During late Proterozoic time, structural flexure of Precambrian basement rock led to the formation of the Tobosa Basin. The Tobosa Basin is an ancient sedimentary basin composed mainly of carbonates fine-grained clastic sediments. Early to Middle Cambrian rocks are absent from the area indicating the Tobosa Basin was above sea level during this time period. As the sea began to transgress, the Late Cambrian Hickory Sandstone Member of the Riley formation was deposited. A shift towards transgressive facies is noted in the overlying Lower Ordovician Ellenburger Group, which consists mostly of limestone and dolomite. Mapping of the Ellenburger shows early architectural features of the Permian Basin. The western edge where the Ellenburger pinches out roughly marks the Diablo Platform. The eastern pinchout of the Ellenburger represents the position of the developing Central Basin Platform. East of the Central Basin Platform, the Tobosa Basin had not yet developed at the time of early Ordovician (Frenzel et al., 1988).

Middle to Late Ordovician deposition consists of the Simpson Group and Montoya Formation. Both the Simpson Group and Montoya Formation are truncated near the Texas Arch which indicates the first appearance of the arch as a positive feature in the Tobosa Basin. Deposition is predominately carbonate from the Late Ordovician through Middle Devonian and is mostly absent of any major structural events or tectonic activity. In Late Devonian time, carbonate deposition diminished in favor of black shales. The Late Devonian Woodford Shale is highly organic and likely acts as an important hydrocarbon source rock in the Permian Basin (Cloud and Barnes, 1948). After deposition of the Woodford black shales in the Late Devonian time, it ceased to exist as an active depositional basin. Hence, the pinchouts of the Woodford represent the extent of the Tobosa Basin.

The Mississippian represented a transitional period for the Permian Basin region. From the Cambrian through Mississippian, the region was mostly stable and absent of tectonism. In the Late Mississippian, tectonism increased significantly as the progressive collision of Laurentia and Gondwana began to shape the region. The Matador Uplift, Central Basin Uplift, Pecos Arch, and Diablo Uplift became prominent features of the region during the tectonic collision of the Pennsylvanian. The foreland of the collision underwent rapid subsidence due to tectonic loading (Miall, 2008).

A broad range of depositional environments existed during the Pennsylvanian due to high tectonism. The Early Pennsylvanian marked the onset of subsidence for both the Midland and Delaware Basins. By the Middle Pennsylvanian, the Permian Basin region had developed its contemporary form (Figure 1) Anticlinal structures associated with extensive faulting developed in the regions. From oldest to youngest, the five series deposited during the Pennsylvanian

include the Morrow, Atoka, Strawn, Canyon, and Cisco. The Midland Basin received relatively low sediment input during the Pennsylvanian. Marine shales were the principal deposit, which were flanked on all sides by carbonates. The primary source of hydrocarbons in the Midland Basin from the Pennsylvanian is the Horseshoe Atoll, a semi-circular structure composed of carbonate buildup.

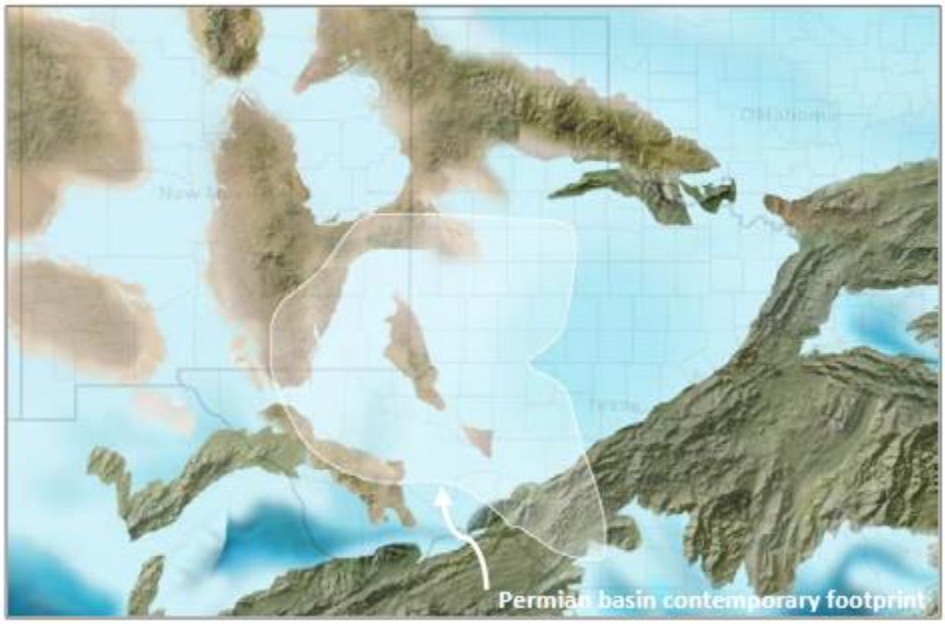

Figure 1: Regional paleogeographic map of the Permian Basin region during the Middle Pennsylvanian (305 Ma) (EIA, 2018).

Deposition of the Wolfcamp shale marks the onset of the Permian Period in the Midland Basin. The Wolfcamp consists mostly of grey shale with interbedded limestone, sourced from debris flow from flanking carbonate buildup. The transition from the Pennsylvanian to the Permian was characterized by rapid subsidence of both the Delaware and Midland basins. The two subsiding basins were separated by the Central Basin Platform which was being rapidly

uplifted during the Early Permian. This uplifting caused differential subsidence between the two basins due to the deferential movements of the basins basement blocks (Oriell et al., 1967). This differential subsidence shaped the basinal dimensions of the Midland and Delaware Basins. Tectonism associated with the Marathon-Ouachita Orogeny began to diminish after the Wolfcampian age. However, subsidence of the basins continued until the end of the Permian Period. Rapid subsidence is evidenced by Wolfcampian deposits reaching approximately 600 meters in the Midland Basin depocenter (Frenzel et al., 1988).

The youngest Leonardian aged is the Dean Sandstone, which conformably overlies the Wolfcamp Shale. The Dean Sandstone is composed of fine-grained quartzose sandstones and siltstones. Overlying the Dean Sandstone is the Spraberry Formation. Similar in lithology to the Dean, this package of rocks is termed the Spraberry Trend. Both the Dean Sandstone and the Spraberry Formation were targeted early in the development of the Permian Basin as a prolific conventional stratigraphic oil play. The primary mode of deposition for the Spraberry Trend was deepwater resedimentation of shelf-derived carbonates and clastic feeder channels (Handford, 1981).

The stratigraphic column of the Midland Basin is presented in Figure 2 (modified from Pioneer, 2014). The Canyon formation is sometimes referred to as the Wolfcamp D. For the purpose of this report, it is referred to as the Canyon formation.

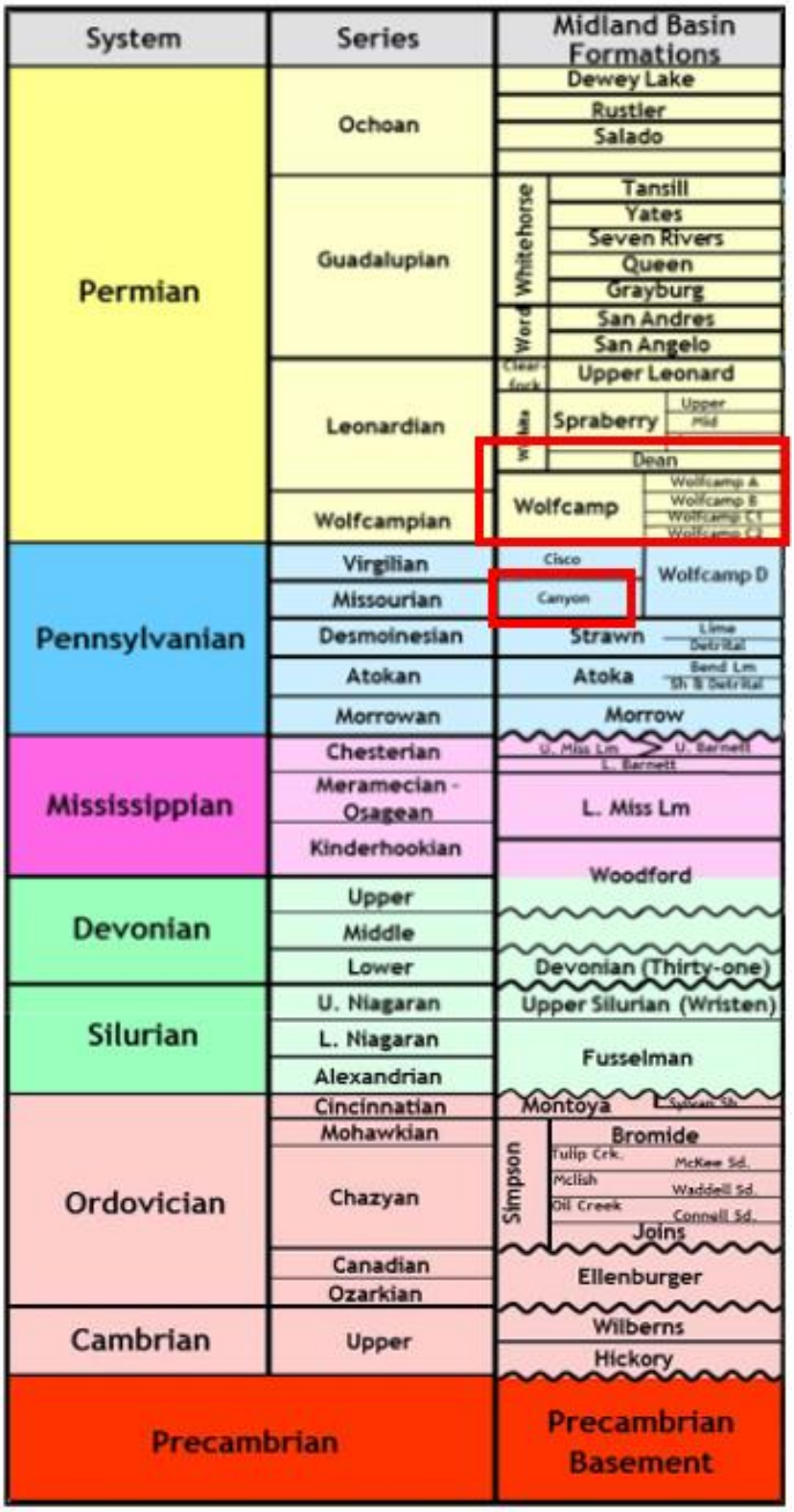

Figure 2: Stratigraphic column of the Midland Basin from Precambrian to Permian; formations studied in this research are boxed in red (modified from Pioneer, 2014).

METHODS

Nanopetrophysical characteristics were studied for ten core samples from three wells in the Midland Basin's Dean, Wolfcamp, and Canyon formations. Table 1 details the core samples tested. Location for each well is provided in Figure 3. Note that API and location of the Wheeler well was not disclosed and is therefore not included. The Wheeler well was drilled in Reagan county, directly to the east of Upton county.

Table 1: Summary of core samples studied

Sample ID	Formation	Age	Rock Type	Well	Depth	County	Operator
W-8203-D	Dean	Permian	Shale	Wheeler	8203	Reagan	Pioneer Natural Resources
W-8279-D	Dean	Permian	Shale	Wheeler	8279.83	Reagan	Pioneer Natural Resources
W-8280-D	Dean	Permian	Shale	Wheeler	8280.83	Reagan	Pioneer Natural Resources
W-8291-D	Dean	Permian	Siltstone	Wheeler	8291.91	Reagan	Pioneer Natural Resources
W-8292-D	Dean	Permian	Siltstone	Wheeler	8292.83	Reagan	Pioneer Natural Resources
ME-8444-WC	Wolfcamp A	Permian	Shale	Mary Ellen #1	8444.84	Upton	Diamondback Energy
ME-8455-WC	Wolfcamp A	Permian	Shale	Mary Ellen #1	8455.15	Upton	Diamondback Energy
ME-8463-WC	Wolfcamp A	Permian	Shale	Mary Ellen #1	8463	Upton	Diamondback Energy
JB-9904-WC	Wolfcamp C	Permian	Shale	James Brown 18-2	9904	Dawson	Diamondback Energy
JB-10570-C	Canyon	Pennsylvanian	Shale	James Brown 18-4	10570.6	Dawson	Diamondback Energy

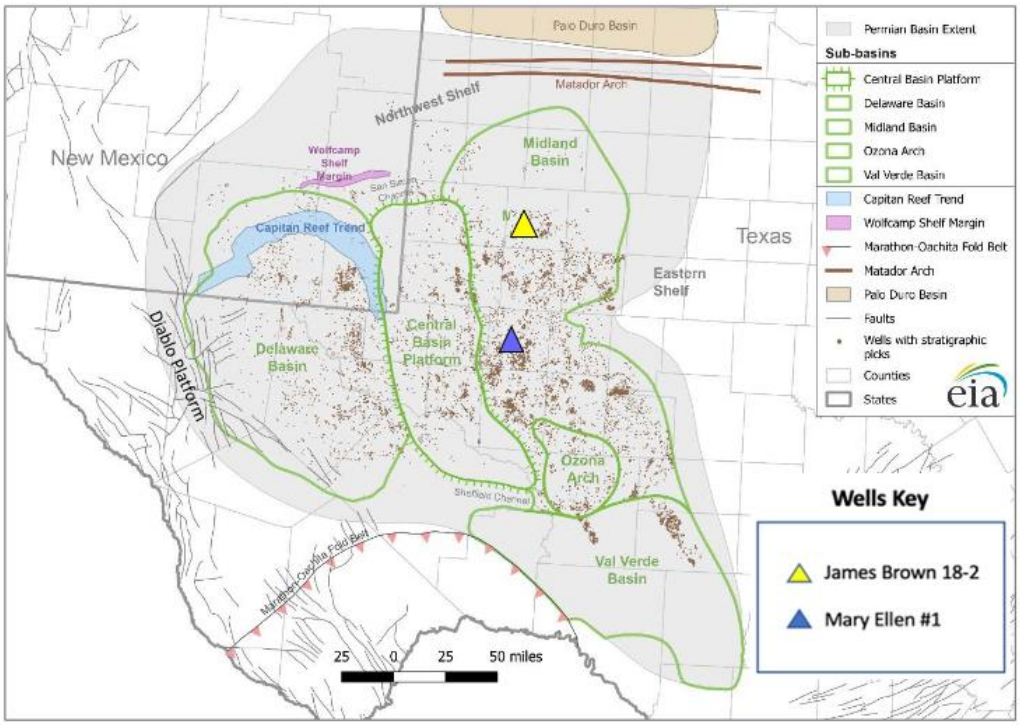

Figure 3: Location of wells used for core samples within the Permian Basin. Modified from EIA (2018).

Sample processing

The samples from the Wheeler well were received as irregular slab samples while the rest of the samples were received as smaller core plugs or crushed sediment. Photographs of the samples in their initial state are provided in the Appendix A.

Core and plug samples were cut into numerous 1 cm^3 cubes using a Hi-Tech diamond saw (Figure 4). These cubes were subsequently cut into 0.5 cm x 1 cm x 1 cm half cube pieces (for SEM imaging) and 0.3 cm x 1 cm x 1 cm thin slabs (for contact angle measurements). After cutting samples into cubes, half cubes, and thin slabs, the remaining sample mass was crushed momentarily using a small mortar and pestle and a FT-120 grinder (Figure 5). The crushed granular sediment was then sorted into the following grain size diameters using sieves: GRI

(500-841 µm-841 µm), Size B (177 µm – 500 µm), Size C (75-177 µm), and powder (<75 µm). Some samples with low initial mass had either limited or no cubes cut. See Table 2 for information on which tests were completed for each sample.

Figure 4: Hi-Tech diamond saw used to cut cores and plugs into cubes and thin slabs

Sample ID	Vacuum Saturation	TOC	Pyrolysis	XRD	Imbibition	Liquid Pycnometry	MICP	Contact Angle
W-8203-D	✓	✓	✓	✓	✓	✓	✓	✓
W-8279-D	✓	✓	✓	✓	✓	✓	✓	✓
W-8280-D	✓	✓	✓	✓	✓		✓	✓
W-8291-D	✓	✓	✓	✓	✓		✓	✓
W-8292-D	✓	✓	✓	✓	✓		✓	✓
ME-8444-WC	✓	✓	✓	✓	✓	✓	✓	✓
ME-8455-WC	✓	✓	✓	✓	✓	✓	✓	
ME-8463-WC	✓	✓	✓	✓	✓	✓	✓	
JB-9904-WC	✓				✓		✓	
JB-10570-WC	✓	✓	✓	✓	✓	✓	✓	

Table 2: Lists of experiments completed for each sample

Figure 5: FT-120 grinder used to crush sample pieces into granular sediment

X-ray diffraction (XRD)

Quantitative mineralogy of the samples was assessed using X-Ray diffraction (XRD). Samples were prepared for XRD by crushing the sample and collecting the powder. Nine samples had sufficient powder mass to test for XRD which requires approximately 1 gram. XRD was performed using the Shimadzu XRD-7000 at the Shimadzu Center for Environmental

Forensics and Material Science at the University of Texas at Arlington. Approximately 1 to 2 mL of powder was gently pressed into aluminum plates containing 25 mm diameter divots. Care was taken to ensure that the sample powder was solely contained within the divots and maintained an approximately even surface with the surrounding sample plate. Once loaded in to the XRD, samples were rotated at 6 rpm and ran from a 2θ of 2° to 70° at a step size of 0.02° and scan speed of 2°/minute with an X-ray (Cu Kα source = 1.5406 Å) accelerating voltage of 40 kV and current of 30 mA. Scans were obtained in approximately 30 minutes. After the scans were collected, they were processed using the MDI Jade9 software package. Sample spectra were compared against the ICDD PDF-4+ 2018 XRD reference spectra database and their mineralogy was modelled using the built-in relative intensity ratio (RIR) method of the Jade9 software.

Geochemistry

Total carbon and inorganic carbon contents, thermal maturity, and kerogen type were determined at GeoMark Research. Maturity can be evaluated using pyrolysis testing. TOC and pyrolysis testing were completed using high-temperature (1200 °C) combustion.

Burial, depositional environment, and diagenesis are reflected in the geochemistry of rocks. Quantifying the geochemical characteristics of shales allows for a better understanding of its nature and history. Most shale formations in USA originated as organic-rich mud being deposited in marine environments. The determination of kerogen type yields insight into a narrower depositional environment, as kerogen types can be linked to specific environments based on hydrogen:carbon ratios. As this organic material is buried, it begins to generate oil or

gas depending on the kerogen type and the burial history. Hydrocarbon generation trends can be interpreted using vitrinite reflectance (R_{oe}), which is a measure of the maturity of organic matter. The relationship between burial and vitrinite reflectance was investigated for the Barnett shale by Jarvie et al. (2001) who established an equivalency correlation between T_{max}, the temperature at maximum evolution of kerogen decomposition, and vitrinite reflection.

It should be noted that the volumetric presence of kerogen is understated by the weight percentage measurement. The volumetric percent of kerogen can double that of the weight percentage (Passey et al., 2010). Predicting zones of high TOC through hydrocarbon generation modeling is critical to shale development.

The methods used by GeoMark Research are provided in Appendix B. The data obtained includes total organic carbon (TOC), vitrinite reflectance (R_{oe}), S1, S2, S3, T_{max}, and kerogen type. These data could be used to infer kerogen type, which is important to assessing a source rocks hydrocarbon quality. The hydrogen index (HI), which represents the amount of hydrogen relative organic carbon in a sample, is calculated using the S2 curve. The oxygen index (OI), which represents the amount of oxygen relative to organic carbon, is calculated using the S3 curve. The relationship between HI and OI yields insight to kerogen type.

Mercury injection capillary pressure (MICP)

Intrusion pressures from mercury injection have been used to estimate pore throat diameters for the past century using the Washburn equation (Washburn, 1921; Equation 1). The intrusion pressure required to overcome the capillary forces yields insight into the diameter of the pore throat. MICP data was analyzed using inflection points (IP) analysis. By

injecting a non-wetting fluid such as mercury into a sample, pressure must build up before it begins to overcome capillary forces and displace the wetting phase. Once this pressure is achieved, there is a rapid intrusion of mercury into the sample. This phenomenon is identified as an inflection point on a log-log plots of differential intrusion volume versus intrusion pressure (Gao and Hu, 2017). At this pressure, mercury is percolating across the sample via the sample's connected pore space. This pressure can be used to calculate the associated dominant pore-throat size. Pressure intrusion utilized in this study ranged from 5 psi (mostly, and 0.2 psi for samples with porosity larger than 3%) to 60,000 psi.

$$\Delta P = \frac{2\gamma}{r} = \frac{2\gamma\cos(\theta)}{r_{pore}}$$

(Equation 1)

where:

ΔP = pressure drop across the pore interface

γ = surface tension of mercury

θ = contact angle between the sample and mercury

r_1 and r_2 = describe the radius of curvature of the pore interface

r_{pore} = pore radius

The relationship between pore-throat size and intrusion is limited by an assumption of constant contact angle and surface tension. When dealing with nanopores, the contact angle is not constant (Hu et al., 2017). The contact angle of mercury increases exponentially with

decreasing pore size. Wang et al. (2016, Equation 2) illustrate a confinement correction for MICP tests performed on shale nanopores that is utilized in this study. Additionally, the surface tension must be adjusted with pores smaller than 20 nm. With these corrections made, intrusion pressures were correlated to pore-throat sizes using Wang's modified Washburn equation:

$$p_c = -\frac{2\gamma_{Hg}(r) * \cos(\theta_{Hg}(r))}{r}$$

(Equation 2)

where:

p_c = mercury intrusion capillary pressure

r = pore-throat radius

$\gamma_{Hg}(r)$ = liquid-vapor surface tension of mercury as a function of pore-throat radius

$\theta_{Hg}(r)$ = contact angle as a function of pore-throat radius

Mercury injection capillary pressure (MICP) tests were performed on 1 cm^3 cubic samples. MICP provides a direct measurement of bulk density, particle density, total pore surface area, porosity, and pore throat diameter distribution. Additionally, MICP data can be used to indirectly estimate the permeability and tortuosity (Hager, 1998). The permeability of pore-throat systems can be approximated using the Katz-Thompson (1987) relationship:

$$k = \frac{1}{89}\,(L_{max})^2\left(\frac{L_{max}}{L_c}\right)\emptyset S(L_{max})$$

(Equation 3)

where:

k =absolute permeability (μm^2)

L_{max} = pore throat diameter at maximum hydraulic conductance (μm)

L_c = characteristic length (i.e. pore throat diameter at threshold pressure P_c) (μm)

P_t = inflection point pressure (Pa)

Φ = porosity (%)

$S(L_{max})$ = mercury saturation at L_{max} (%)

The assessment of permeability is complicated by the existence of multiple pore-throat systems which contribute to fluid flow. Equation 2 is a measurement of permeability for only one pore-throat diameter. Rezaee et al. (2006) concluded that the median pore-throat diameter yields the best approximation for permeability in carbonate rocks. The procedure outlined by Gao and Hu (2013), who utilized median pore-throat diameters to calculate permeability in shale samples, is utilized in this study to estimate permeability (k_{GH}). This method uses only the median pore throat. Additionally, both permeability and tortuosity were calculated separately for two pore-throat networks: >100 nm (k_{100}) and 2.8-50 nm ($k_{2.8\text{-}50}$). Permeability in the 2.8-50 nm range, $k_{2.8\text{-}50}$, might better characterize flow through organic matter-hosted pore network.

Shale porosity can be subdivided into three groups: interparticle, intraparticle, and organic porosity. Organic porosity is pore space that exists within the organic material. It is

thought to be created by the compaction and maturation of kerogen. Typically, pore space housed within organic material exhibits oil-wet behavior. Reed and Loucks (2015) estimate that pore space between mineral grains, or intergranular porosity, can range from nanometers to micrometers. Interparticle porosity associated with clay is known to cause problems in determining porosity. This inter-clay pore space, which is on the nanometer scale, are subject to great capillary force. This phenomenon leads to clay-bound water, hydroxyl ions stuck to the octahedral sheets of clay. Whether or not clay-bound water should contribute to the total porosity is a subject of debate (Passey et al., 2010). Intraparticle porosity is pore space that is created within mineral grains. Intraparticle porosity commonly results from the dissolution of grains and unstable rock fragments. Typically on the micrometer scale, microfractures associated with grain boundaries can contribute to the porosity of rocks. An idea of organic porosity fraction can be estimated by quantifying cumulative mercury intrusion percentage at pore diameters associated with organic pores. Pommer and Milliken (2015) studied pore-size distributions of different pore types in the Eagle Ford FE-SEM (field emission-scanning electron microscopy) imaging. Their research showed that organic pore space has an average value of 13.1 nms, considering the detection limit of 5 nm for FE-SEM. Quantification of inorganic vs. organic porosity requires imaging (e.g. FE-SEM) and is beyond the scope of this paper. However, a general approximation of organic porosity pore diameter range of 10-50 nm is recognized.

Wettability and contact angle

Wettability describes the preference of a solid to be in contact with one fluid over another fluid. Wettability has been noted as an important reservoir characteristic with

significant impact on fluid flow. Shale systems are unique in that that they may exhibit "Dalmatian" wettability (Hu et al., 2017). Dalmatian wettability refers to the dual wettability of shale: organic matter contained within shale is typically oil-wet while the minerals are water-wet. Both the organic matter and mineral wettability can be altered in diagenesis. Figure 6 demonstrates the fundamental principle of measuring wettability by contact angle. If a fluid droplet exhibits 0° contact between a surface, the surface is wetting to the fluid. If a fluid droplet exhibits 180°, or beads up, the surface is non-wetting to the fluid.

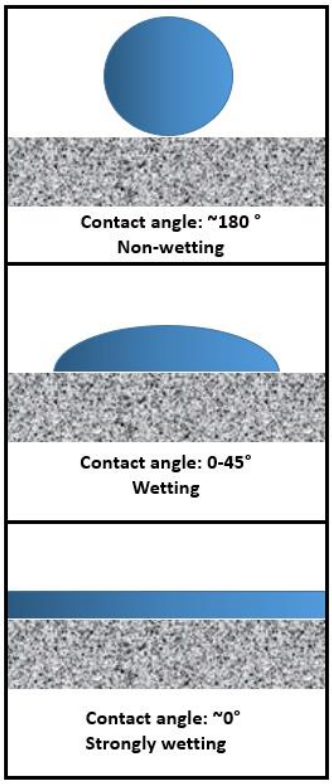

Figure 6: Wettability of a surface to a fluid by measuring contact angle. 0° represents the most non-wetting fluid while 180° represents the most wetting fluid.

In order to determine the wettability of the samples, thin slabs were cut from the sample and polished. These thin slabs were approximately 2mm x 10mm x 10 mm. Samples were tested for wettability to DIW, n-decane, 20% THF in water, and API brine (8 wt% NaCl + 2 wt% $CaCl_2$). The contact angle between these fluids and the samples were determined using the USA KINO SL200K contact angle meter and interfacial tensiometer (Figure 7). This machine is capable of measuring the contact angle between the droplet and the surface with respect to time. The data was then collected and used to determine wettability.

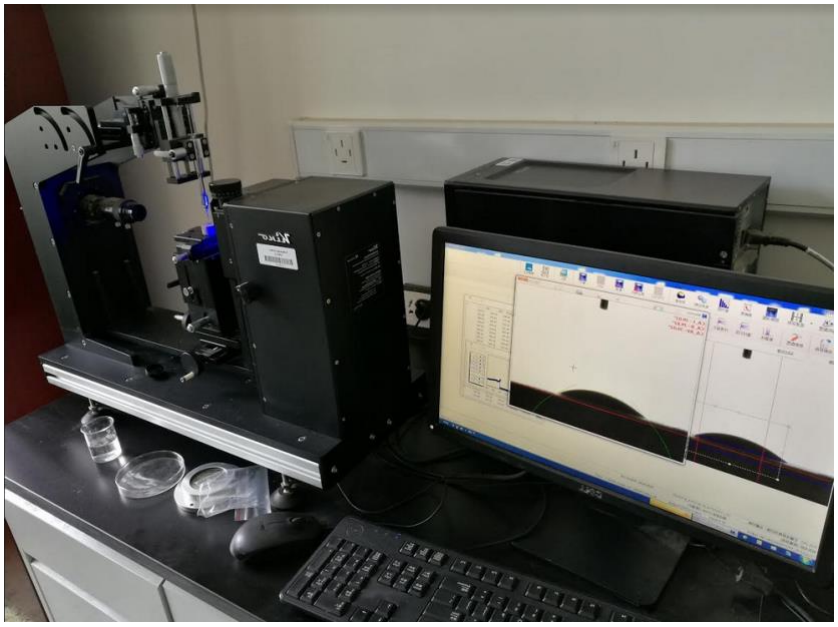

Figure 7: USA KINO SL200K contact angle meter and interfacial tensiometer used to determine sample wettability.

Vacuum saturation

Vacuum saturation and liquid displacement methods were used to determine the porosity of the samples. There are numerous tests available for pore characterization including MICP, liquid and gas diffusion tests, Ar ion milling, small-angle neutron scattering and more.

Using vacuum saturation and liquid displacement to study pore structure is cost-effective and allows for large, irregular samples to be tested. The goal of vacuum saturation is to measure edge-accessible porosity, bulk density, and grain density. Edge-accessible porosity is analogous but different to effective porosity. Figure 8 illustrates different types of porosity in shale samples. Edge-accessible porosity includes both edge porosity and infinite cluster porosity. Both edge porosity and infinite cluster represent pore space that would theoretically contribute to fluid flow from the shale matrix towards the induced fracture network.

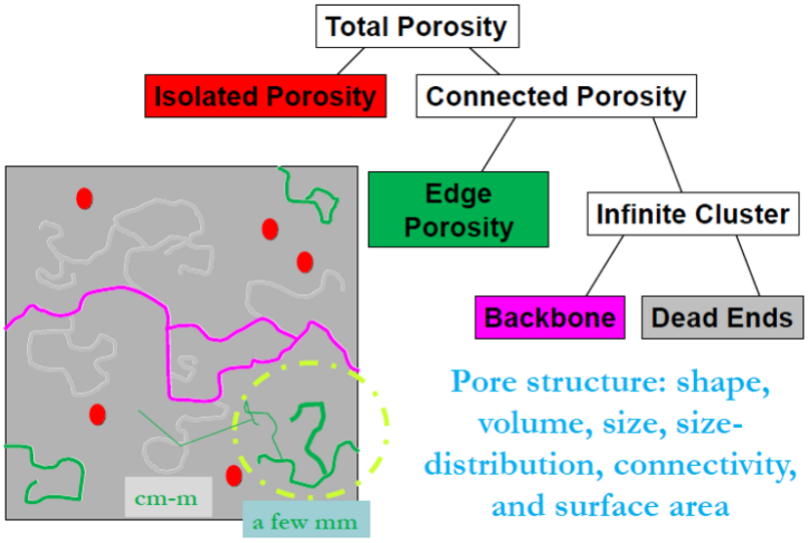

Figure 8: Pore network observed in shale rocks consists of both isolated and connected porosity. Laboratory methods such as vacuum saturation might not detect isolated porosity (Hu, 2010).

Pore structure is assessed by evacuating the accessible pores of the sample by immersing the sample in fluid and pressuring it with compressed CO_2 gas. By weighing samples prior to and after saturation, the total mass of the fluid saturated into the accessible pores of the sample can be determined and used to calculate the accessible pore volume.

Saturating fluids of contrasting wettability were used during vacuum saturation. Using fluids with different wettability allows for the effect of the sample's wettability to be examined. Deionized water (DIW), DT2 (2:1 ratio of n-decane and toluene) and tetrahydrofuran (THF) are used as saturating fluids. DIW is water-wet while DT2 is oil-wet. THF has neutral wettability.

The apparatus consists of the sample chamber connected to a vacuum pump, compressed CO_2 container, and a fluid reservoir. An illustration of the experiment set-up is shown in Figure 9.

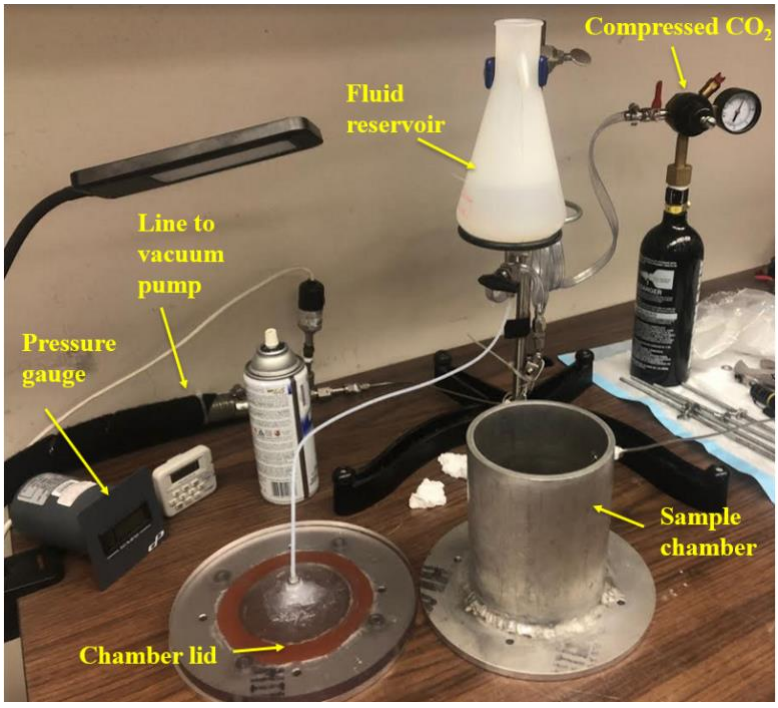

Figure 9: Photo of vacuum saturation experiment set-up.

Procedure

Samples tested by vacuum saturation are listed in Table 4. Vacuum saturation was completed for cores and 1 cm^3 cubes. Prior to the experiment, samples are placed in a 60 °C oven for 48 hours. The dry samples are then weighed and recorded.

Sample ID	DIW		DT2	THF
	Slab	1 cm^3 cube	1 cm^3 cube	1 cm^3 cube
W-8203-D	✓	✓✓✓	✓	✓
W-8279-D	✓	✓✓✓	✓	✓
W-8280-D	✓	✓✓✓	✓	✓
W-8291-D	✓	✓✓✓	✓	✓
W-8292-D	✓	✓✓✓	✓	✓
ME-8444-WC		✓✓✓	✓	✓
ME-8455-WC		✓✓✓	✓	✓
ME-8463-WC		✓✓✓	✓	✓
JB-9904-WC		✓✓✓	✓	✓
JB-10570-C		✓✓✓	✓	✓

Table 3: DIW, DT2, and THF vacuum saturation trials performed for each sample form.

Step 1) Evacuation

The saturating fluid was prepared for DIW by de-airing and boiling DIW. Enough fluid must be prepared to fill the entire ~500 mL sample chamber. The DIW was then cooled to room

temperature before use. Large, irregular dried samples are simply placed in the chamber. However, for 1 cm cube runs, an aluminum sample rack was custom-made to keep track of each sample (Figure 10). With the samples placed in the sample chamber, the chamber lid was then sealed. A three-way valve connecting the vacuum, compressed CO_2 gas, and sample chamber was then opened to allow flow between the vacuum and sample chamber. The vacuum pump was then turned on, while the pressure in the chamber was recorded. The chamber was then allowed to evacuate for 8-12 hours. After this time period, the 3-way valve was opened towards the compressed CO_2 gas cylinder and the vacuum pump was turned off. CO_2 was then introduced to the sample chamber at 50 psi in order to displace residual air in the sample. The pressurized sample was then disconnected from both the vacuum pump and the gas cylinder. CO_2 was released into the chamber for 30 minutes. A vacuum was pulled for 120 minutes. CO_2 was once again released into the chamber for 30 minutes, followed by another period of vacuum pulling for 8-12 hours.

Figure 10: Aluminum rack used during vacuum saturation to keep samples organized

Step 2) Introducing Fluid

With the samples evacuated, the saturating fluid can be introduced into the sample chamber. The sample chamber was filled sufficiently to entirely submerge the samples. This was achieved by using a fluid reservoir which was connected to the sample chamber by tubing. The CO_2 pressurization steps described above were repeated, driving fluid into the accessible pores of the sample. The sample chamber pressure throughout this step was recorded.

Step 3) Weighing saturated samples

The sample lid was disconnected and the chamber was taken to an analytical balance. Care was taken to keep the samples submerged while other samples were being measured.

Each sample was weighed twice after gently wiping the surfaces of the sample with a moist Kimwipe. Additionally, the sample was weighed in a bucket filled with the saturating fluid. Using Archimedes method as outlined by API (1998), samples were weighed in a bucket of the saturating fluid. The bucket was placed on an analytical balance and filled with the saturating fluid. A cradle apparatus allowed for lowering the sample into the bucket. With the bucket filled and the cradle submerged, the analytical balance was tarred. The sample was then placed in the cradle, providing a submerged weight of the sample. This process is illustrated in Figure 11.

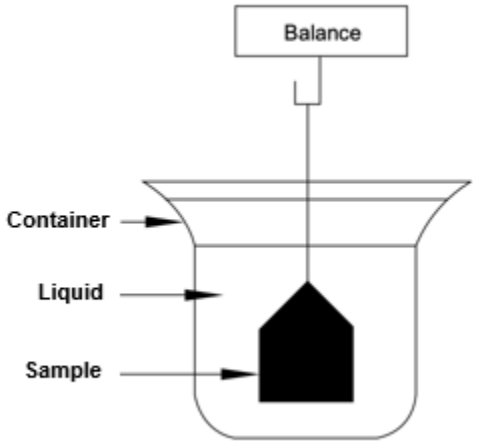

Figure 11: Illustration of Archimedes bucket used to determine submerged weights. This method is utilized in the calculation of pore volume after vacuum saturation. (API, 1998)

The porosity of the sample can then be calculated with the following equations:

$$V_f = \frac{W_{ss} - W_{ds}}{\rho_f}$$

(Equation 4)

where:

V_f = volume of fluid contained in vacuum saturated sample (cm^3)

W_{ss} = weight of vacuum saturated sample (g)

W_{ds} = weight of oven-dried sample (g)

ρ_f = density of saturating fluid (g/cm^3)

$$V_b = \frac{W_{ssa}}{\rho_f}$$

(Equation 5)

where:

W_{ssa} = weight of the saturated sample as measured in fluid (using Archimedes bucket) (g)

V_b = bulk density (g/cm^3)

Porosity can then be calculated:

$$Porosity = \frac{V_f}{V_b}$$

(Equation 6)

Fluid imbibition

Spontaneous imbibition is a phenomenon where a nonwetting fluid is displaced by a wetting fluid due to capillary pressure. Imbibition is an important process for formation evaluation and enhanced oil recovery as it affects fluid migration through porous media. Here, the principles of spontaneous imbibition were utilized to characterize the connectivity and wettability of the pore-throat system of test samples.

Hu et al. (2012) demonstrated that pore connectivity in natural rock cause anomalies in imbibition slopes [log (cumulative imbibition) vs log(imbibition time)]. Their research models fluid flow in low connectivity rock using percolation theory, which describes how macroscopic properties emerge from microscopic pore connections. In rocks with low pore connectivity, anomalous diffusion is expected to occur. Ewing and Horton (2002) showed that poorly-connected rocks do not exhibit classical diffusion: the imbibition slopes for poorly connected rocks are typically lower than the classical diffusion value of 0.5, exhibiting imbibition slopes of around 0.25. Drawing from this, the methods here include plotting the logarithm of cumulative imbibition versus the logarithm of imbibition time, where the resulting imbibition slope can be used to draw insights into pore connectivity.

The rate of fluid imbibition into samples was measured using the following methods. First, 1 cm^3 cubes were epoxied on four sides leaving only the two sides parallel to the bedding planes exposed. Epoxy is used in this way to limit vapor adsorption through the sides of the sample. Dry sample weights are recorded by measuring weights after a 48-hour period in a 60 °C oven. Fluid imbibition tests were completed using both DIW and DT2 fluids. A fluid reservoir was filled up with either DIW or DT2 fluid depending on the test. This fluid reservoir was then placed within a plastic chamber. Separate containers filled with the imbibition fluid were placed in the plastic chamber to maintain a high relative humidity. The oven dried sample were then weighed and placed in a sample holder that was suspended from an analytical balance. The experimental setup is illustrated in Figure 12. An adjustable stage was utilized to raise and lower the fluid reservoir. This stage is lifted in order to place the water edge in contact with the exposed sample surface. Once contact is made, the logging software of the analytical balance

begins to record weight changes of the suspended sample. The logging software records weights for a 24-hour period according to a specified intervals. In order to avoid excessive inputs, the frequency of the measurement intervals were decreased throughout the duration of the test.

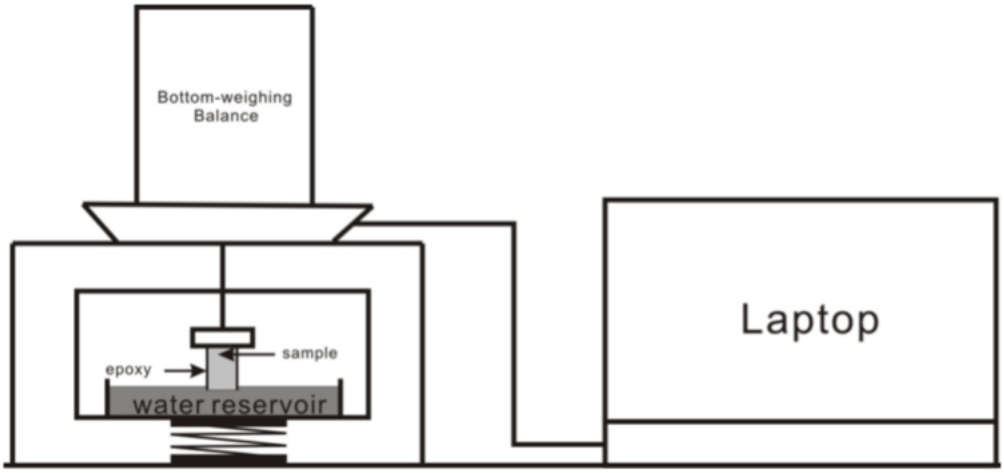

Figure 12: Schematic for the imbibition test apparatus (Gao & Hu, 2012)

At the end of the 24-hour period, the balance reading was recorded. The adjustable stage was lowered and the sample was removed from the chamber. Once removed, the sample was blotted with a damp Kimwipe. The Kimwipe was weighed before and after blotting in order to determine the amount of fluid removed from the sample. This step was performed in order to remove fluid that was not imbibed into the sample but only adhering to the edge. The sample, sample holder, and fluid reservoir were then individually weighed.

Data was processed according to Hu et al. (2001), which recognized that the change in buoyancy force during imbibition results in significant error. As the test progresses and water

imbibed and evaporated from the fluid reservoir into the sample, the buoyancy force on the sample from the fluid reservoir decreased. As the buoyancy force supporting the sample decreased, the balance reading increased. This effect must be quantified and corrected when determining the amount of fluid imbibed into the sample. The buoyancy correction detailed by Hu et al. (2001) was utilized in this research.

Liquid pycnometry

The proportion of edge-accessible porosity present in a sample should be affected by the surface-area-to-volume ratio (SAVR) of the sample. A sample with high SAVR should have a higher proportion of pore space accessible to the surface (edge-accessible) relative to a sample with lower SAVR. The SAVR of spheres decreases with increasing volume. Assuming granular samples are approximately spherical, larger sample sizes should have lower SAVR. If larger sample sizes have lower edge-accessibility to pore space, then the density measurements by liquid displacement should show a divergence at some sample sizes. The presence of edge-accessible porosity is important in shale because the production of shale hydrocarbon is reliant on induced fractures. If shale pore-systems are not characterized by connected edge-accessible pores then fluid flow to the fracture may be limited. Figure 8 illustrates edge-accessible and isolated porosity.

In order to investigate this phenomena, the liquid displacement density measurements were performed for different sample size designations. Tested granular sample sizes include the following designation in our research laboratory: GRI, B, C, and powder. Table 4 provides the sample size dimensions and the associated equivalent spherical diameter.

Size designation	Size	Size	Equivalent spherical diameter (µm)
Irregular	Irregular	~4.0 cm across	68800
Cube	Cube (1 cm side)	Cube (1 cm side)	6204
GRI	Mesh -20/+35	500 - 841 µm	671
Size B	Mesh -35/+80	177 - 500 µm	339
Size C	Mesh -80/+200	75 - 177 µm	126

Table 4: Sample size designation and dimensions for forms tested with liquid pycnometry.

Liquid displacement was performed using DIW, DT2, and THF fluids. Density was calculated using both the weight and volume of displaced fluid. If the edge-accessible pore system is influenced by wettability, the displaced fluid will vary depending on the wettability of the fluid used. Therefore, some variations in apparent bulk density will be noted.

The particle density method outlined by Flint and Flint (2002) was utilized in this study. After samples are crushed and sieved into GRI, B, C, and powder sizes, the samples were placed into a 60 °C oven to dry for at least 48 hours. The experimental setup consists of 10 mL stoppered glass vials (called pycnometers) and an analytical balance (with an error margin of 0.1 mg).

After the samples have been dried, the stoppered glass vials were cleaned and weighed. Next, sediment for each grain size of each sample was weighed out from anywhere between 2.0000g-2.0010g. After this amount of granular sample was obtained, the weight was recorded and placed into the pycnometer. The pycnometer and sediment were weighed. Next, the pycnometer was filled to the top with de-aired DIW. The stopper was then inserted into the pycnometer carefully, forcing excess water out of the capillary. The pycnometer containing DIW

and granular samples was then weighed after thoroughly cleaning the outside of the pycnometer (Figure 13).

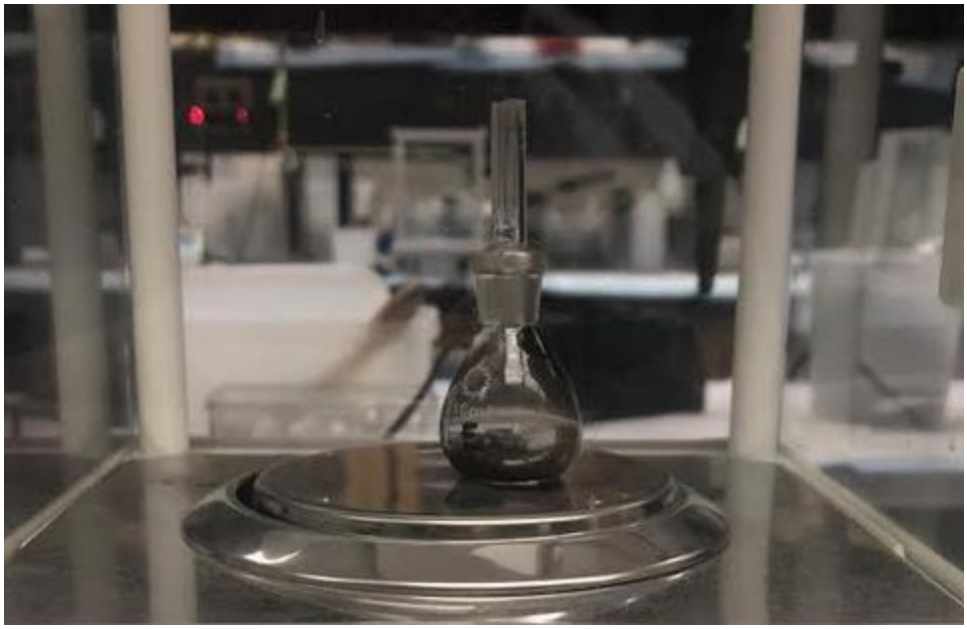

Figure 13: Pycnometer filled with de-aired deionized water and granular samples. Used during liquid pycnometry to determine apparent bulk density for granular samples.

Lastly, the sediment and DIW were removed from the sample. The sample was then refilled with only DIW and weighed. This process was repeated using both DT2 and THF instead of DIW. Each test for each sediment size was duplicated three times using DIW and two times each for both DT2 and THF. The samples tested using liquid pycnometry were selected based on porosity measurements obtained from vacuum saturation. With the porosity values, samples were chosen that covered the full range of porosity values observed in this study. The apparent bulk density was then calculated using the following calculations:

$$Apparent\ bulk\ density = \frac{W_s}{\frac{W_{vf} + W_{vfs} + W_s}{\rho_f}}$$

(Equation 7)

where:

W_s = Weight of the sample (g)

W_{vf} = Weight of the vial containing fluid

W_{vfs} = Weight of the vial containing flui d and sediment

P_f = density of the fluid

RESULTS

X-ray diffraction (XRD)

The mineralogical composition of each sample are shown in Figure 14. A shale classification ternary diagram, modified from Schlumberger (2014), was used to interpret the results. The Dean samples show significantly more quartz and feldspar than the Wolfcamp and Canyon samples. The nine samples tested have approximately similar clay proportions. The Wolfcamp samples exhibit higher carbonate proportions relative to the Dean samples. Quantitative mineralogical results are shown in Table 6.

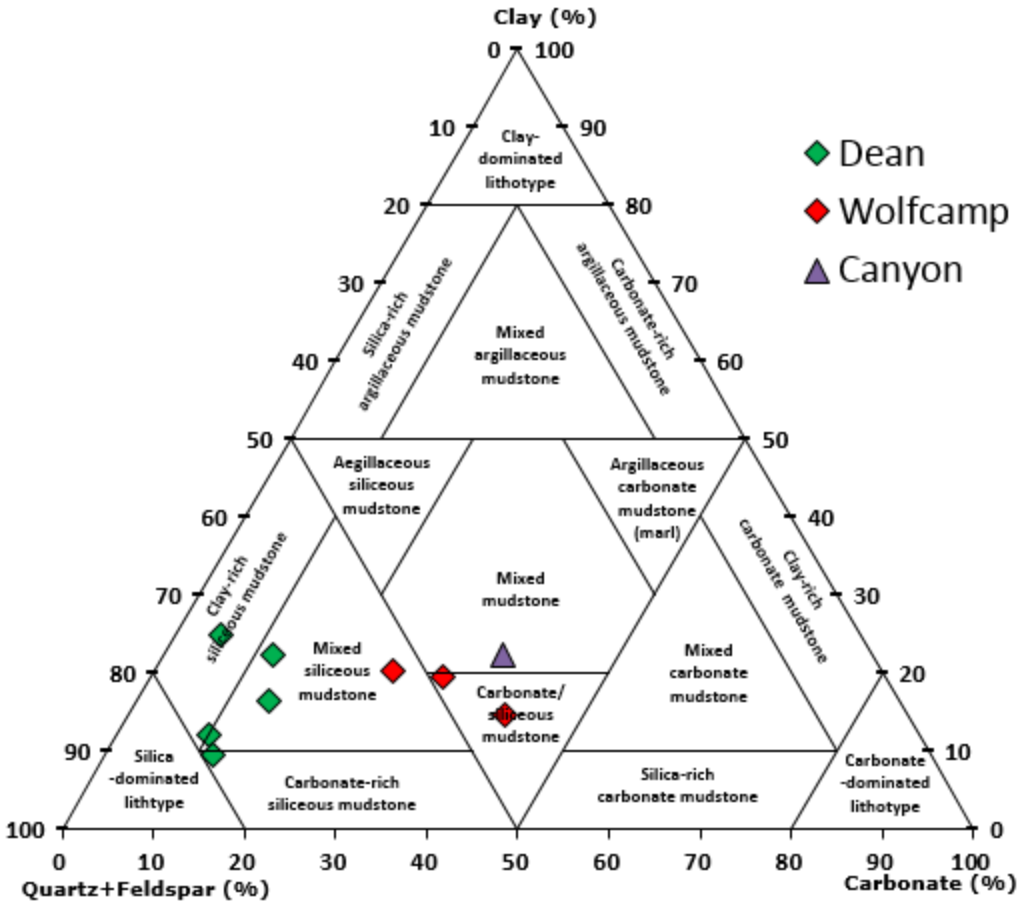

Figure 14: Mineralogical composition of test samples from X-ray diffraction (XRD) results. Plotted with a shale classification ternary diagram (modified from Schlumberger, 2014)

Phase	Type	W-8203-D		W-8279-D		W-8280-D	
		wt.%	±	wt.%	±	wt.%	±
Quartz	*Silica*	47.7	2.8	45.7	2.8	46.3	2.7
Anorthite	*Feldspar*						
Albite	*Feldspar*	17.2	1.1	15.5	1	14.6	0.9
Microcline	*Feldspar*					1.7	0.2
Calcite	*Carbonate*						
Dolomite	*Carbonate*	13.7	0.9	11.2	0.9	4.4	0.4
Fluorapatite	*Phosphate*						
Anhydrite	*Sulfate*	3.5	0.4	2.6	0.3	2.6	0.3
Pyrite	*Sulfide*	2.4	0.3			4.7	0.6
Ulvospinel	*Oxide*			4.2	0.5	3.6	0.4
Illite	*Clay – Mica Group*	15.5	1	20.8	1.6	22.2	1.3
Montmorillonite	*Clay - Smectite Group*						
Clinochlore	*Clay – Chlorite Group*						

Phase	Type	W-8291-D		W-8292-D		ME-8444-WC	
		wt.%	±	wt.%	±	wt.%	±
Quartz	*Silica*	58.2	3.5	56.5	3.4	39.5	2.3
Anorthite	*Feldspar*			1	0.1		
Albite	*Feldspar*	16.2	1	16.1	1.1	9.1	0.7
Microcline	*Feldspar*	3	0.3	3.5	0.3		
Calcite	*Carbonate*					17.4	1.1
Dolomite	*Carbonate*	10.1	0.7	11.5	0.7	6.3	0.5
Fluorapatite	*Phosphate*					2.6	0.3
Anhydrite	*Sulfate*	0.4	0.1	1	0.1		
Pyrite	*Sulfide*			0.8	0.2	3.2	0.3
Ulvospinel	*Oxide*					3.4	0.4
Illite	*Clay – Mica Group*	12.1	0.9	9.5	0.7	18.4	1.5
Montmorillonite	*Clay - Smectite Group*						
Clinochlore	*Clay – Chlorite Group*						

Phase	Type	ME-8455-WC		ME-8463-WC		JB-10570-C	
		wt.%	±	wt.%	±	wt.%	±
Quartz	*Silica*	36	2.1	38.3	2.2	33.7	1.7
Anorthite	*Feldspar*					3.5	0.2
Albite	*Feldspar*	5.1	0.4	7.4	0.5		
Microcline	*Feldspar*						
Calcite	*Carbonate*	30.5	1.8	17.3	1	21.6	1.1
Dolomite	*Carbonate*	7.9	0.6	12.8	0.8	12.4	0.7
Fluorapatite	*Phosphate*	1.9	0.2				
Anhydrite	*Sulfate*			1.7	0.2		
Pyrite	*Sulfide*	2.3	0.3	2	0.2	4	0.3
Ulvospinel	*Oxide*	2.6	0.4	1.9	0.3		
Illite	*Clay – Mica Group*	13.7	1.2	18.6	0.9	24.1	1.7
Montmorillonite	*Clay - Smectite Group*					0.3	0.1
Clinochlore	*Clay – Chlorite Group*					0.4	0.1

Table 5: Quantitative mineralogy of Dean, Wolfcamp, and Canyon samples.

Geochemistry

Pyrolysis and TOC results from test samples are presented in Table 6. The Wolfcamp exhibits the highest TOC percentages relative to the Dean and Canyon samples. Kerogen type was determined using both a Pseudo Van Krevelen plot (Figure 15) and a kerogen quality plot (Figure 16). All samples show mixed type II and type III kerogen. Figure 17 shows all samples are in the oil generation window. It appears the Dean samples have more type III kerogen influence compared to the Wolfcamp and Canyon samples. Vitrinite reflectance was estimated using its relationship with T_{max} (Jarvie et al., 2001).

Sample ID	TOC (%)	S1 (mg HC/g)	S2 (mg HC/g)	S3 (mg CO2/g)	Tmax (°C)	R_{oe} (%)
W-8203-D	0.91	0.38	1.45	0.35	444	0.83
W-8279-D	0.31	0.12	0.27	0.31	440	0.76
W-8280-D	0.3	0.12	0.33	0.27	442	0.8
W-8291-D	0.11	0.09	0.13	0.46	437	0.71
W-8292-D	0.33	0.14	0.54	0.51	449	0.92
ME-8444-WC	3.97	1.99	10.07	0.52	444	0.83
ME-8455-WC	1.69	0.85	3.82	0.41	453	0.99
ME-8463-WC	1.89	1.31	4.14	0.44	444	0.83
JB-10570-C	1.37	0.53	3.25	0.27	441	0.78

Table 6:Pyrolysis and TOC data for test samples.

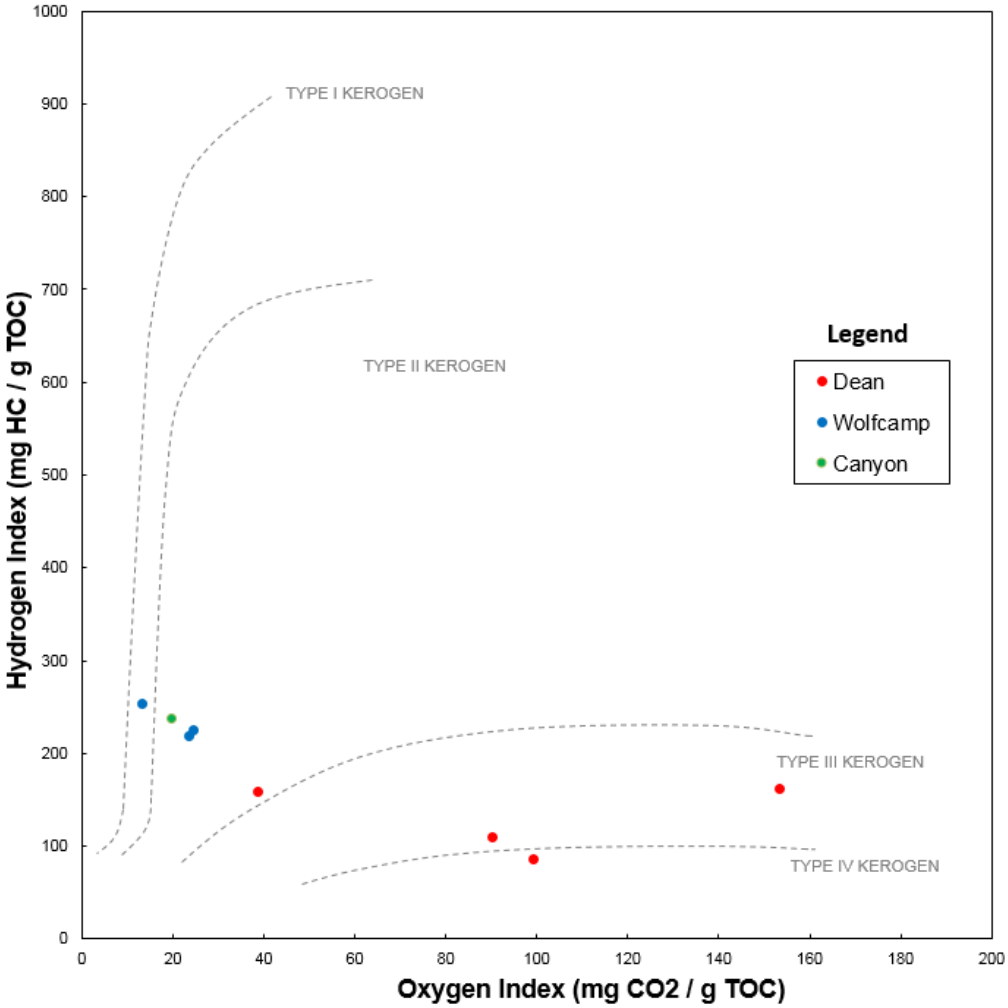

Figure 15: Pseudo Van Krevelen used to interpret kerogen type from pyrolysis testing.

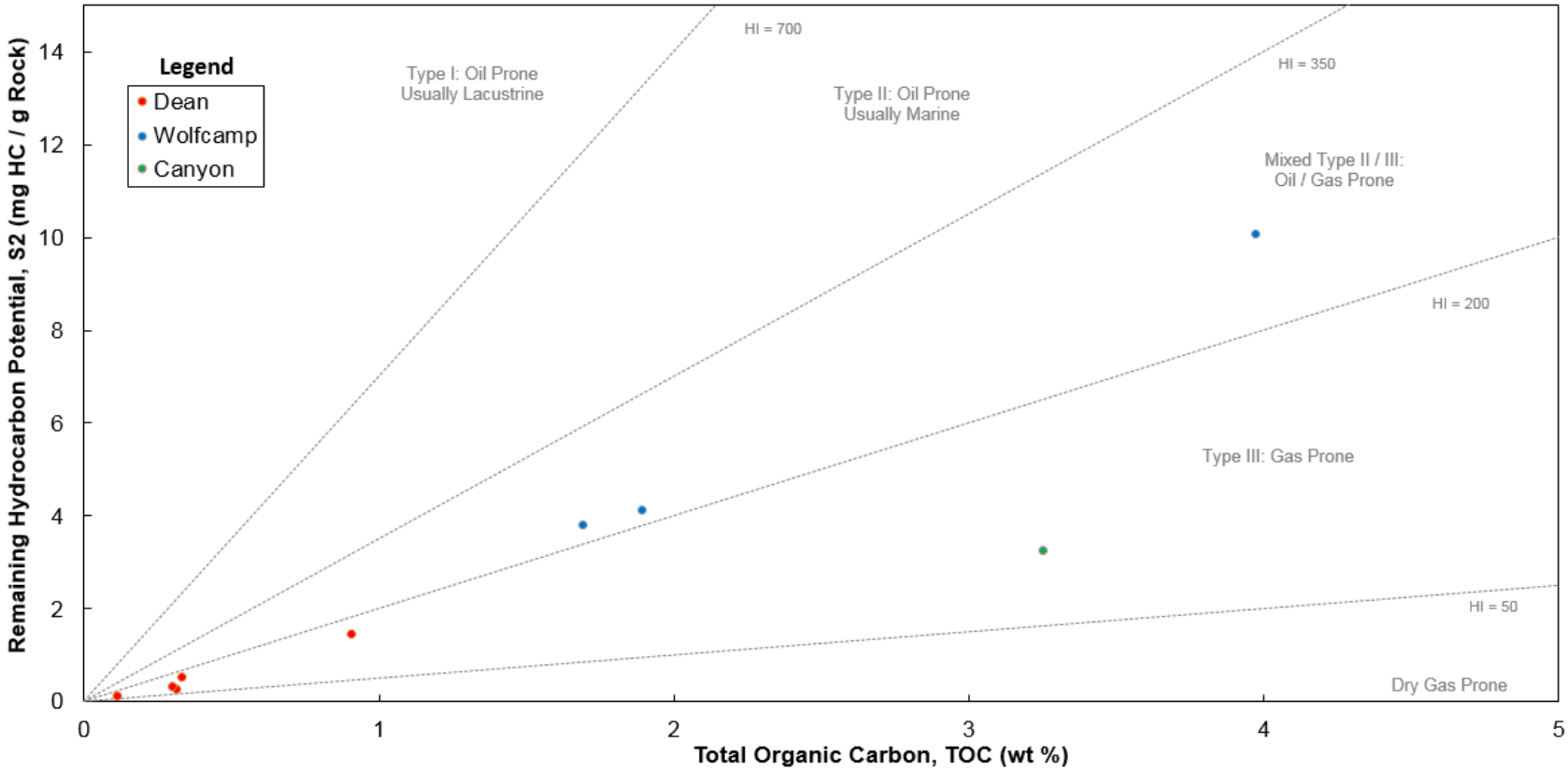

Figure 16: Kerogen quality plot showing estimated kerogen type, depositional environment, and hydrocarbon phase.

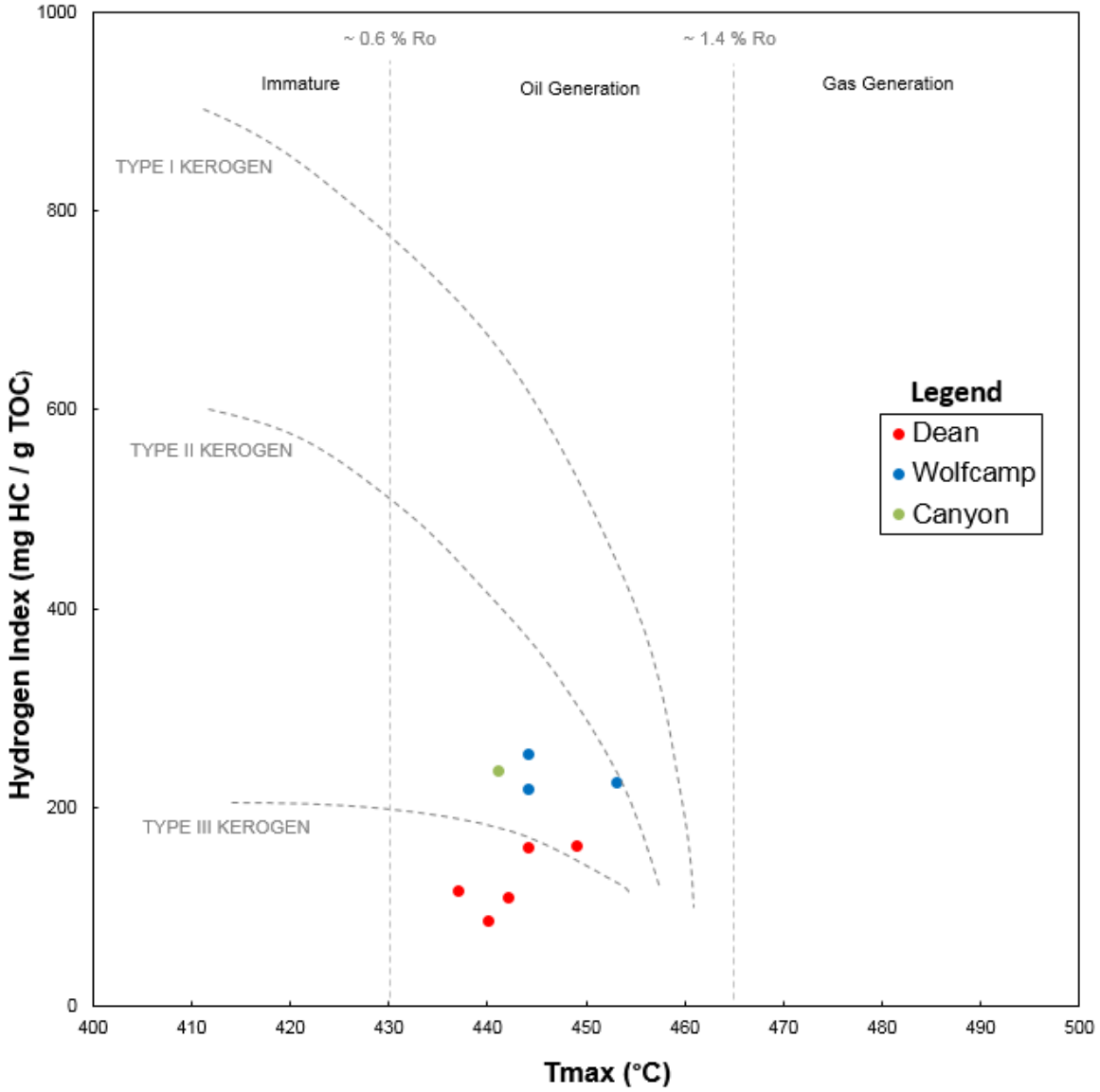

Figure 17: Kerogen type and maturity estimation from pyrolysis data

Mercury injection capillary pressure (MICP)

For most samples run with intrusion pressures from 0.2 to 60000 psi, seven inflection points were identified on log-log plots of differential intrusion volume versus intrusion pressure

(Figure 18). Inflection points are identified with arrows. These seven inflection points are qualitatively associated with different pore types recognized in shales. The upper y-scale separates different pore throat region diameters, each potentially characterized by different types of porosity.

The porosity, bulk and skeletal density calculated from MICP analysis are shown in Table 7. Porosity values for the Dean Formation are all higher (7.95-8.78%) than those of the Wolfcamp Formation(1.69-4.56%). The Canyon sample porosity, 6.54%, was between the Dean and Wolfcamp porosity ranges. Median pore-throat diameter and average pore-throat diameter are provided in Table 8. The percentages of each pore-throat region's share of the total pore throat volume of each sample are provided in Table 9 and Figure 19. All of the Wolfcamp and Canyon samples have dominant pore networks constrained by pore-throats over 100 nm. Samples W-8203-D, W-8279-D, and W-8280-D each have dominant pore-throat networks between the range of 2.8 to 50 nanometers.

The permeability (k_{GH}) calculated using the median pore throat diameter (Gao and Hu, 2013) are compared with k_{100}, $k_{2.8\text{-}50}$, and k_{100} values in Table 10. Focused on the low range of pore-throat sizes which could be predominantly related to OM-hosted pores, $k_{2.8\text{-}50}$ values were lower for each sample relative to both k_{100} and k_{GH}. k_{GH} was higher than k_{100} for the Wolfcamp samples but not for the Dean samples.

Samples with high intrusion volume under 5 psi (i.e. approximately >50 μm by Washburn equation) were processed with an additional method which separated cumulative intrusion using two different regions: >50 μm and <50 μm. Porosity calculated using this method is presented in Table 11.

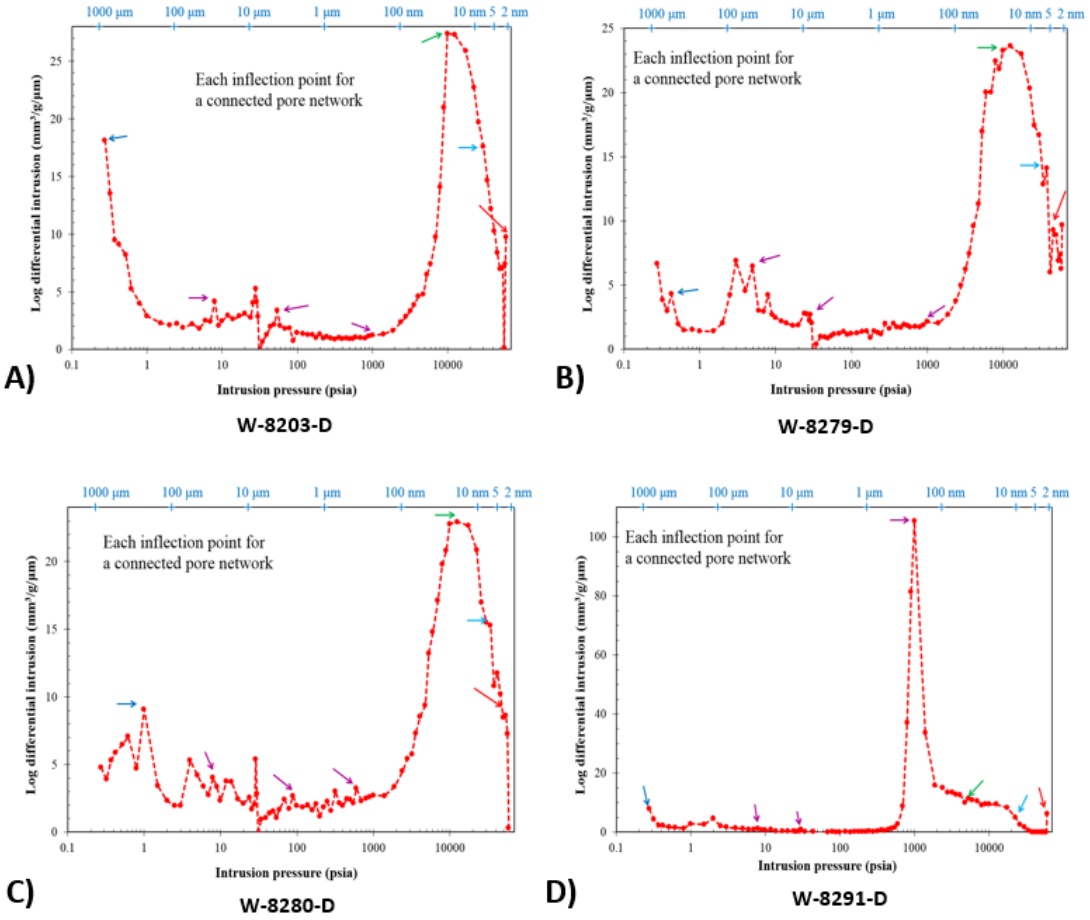

Figure 18: Log-log plot of incremental intrusion mercury volume versus intrusion pressure. Inflection points are indicated by arrows. The upper y-scale separates different pore-throat diameter regions, each potentially characterized by different types of porosity

Figure 18 (cont.):

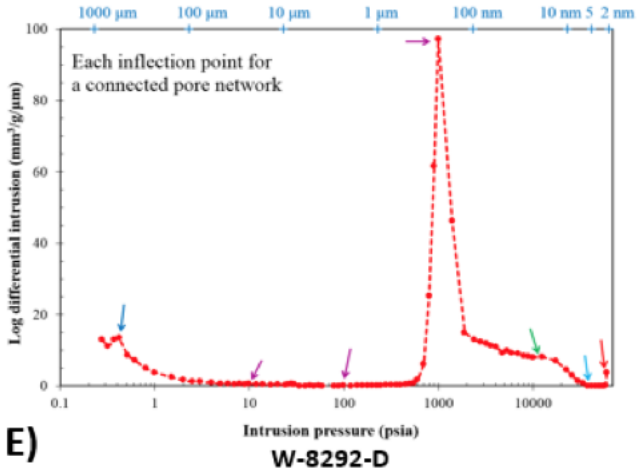

E)
W-8292-D

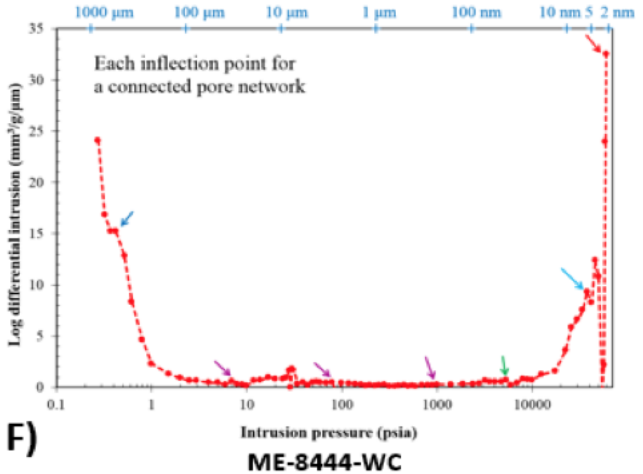

F)
ME-8444-WC

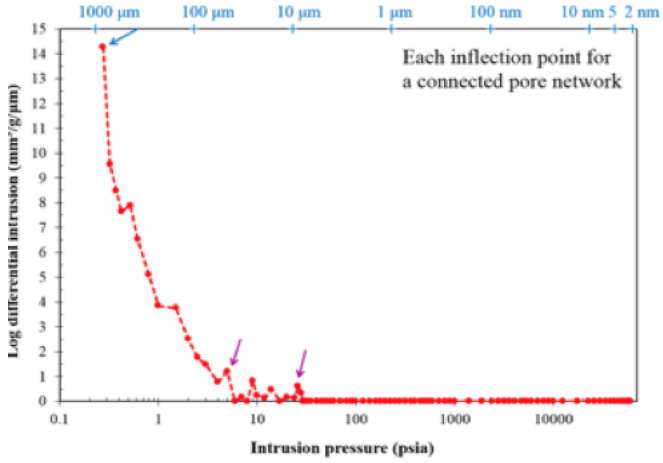

G)
ME-8455-WC

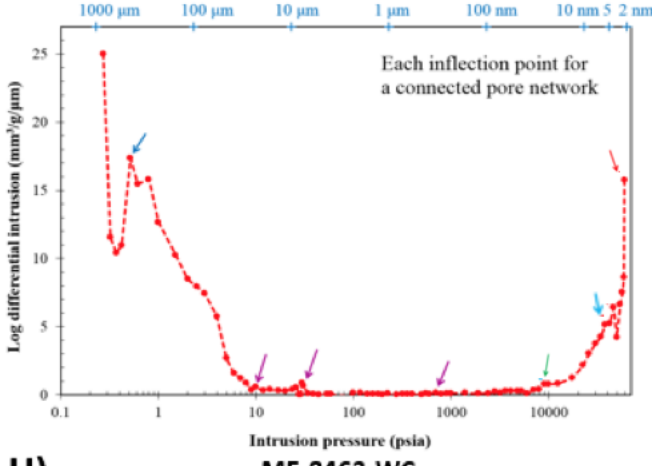

H)
ME-8463-WC

Figure 18 (cont.):

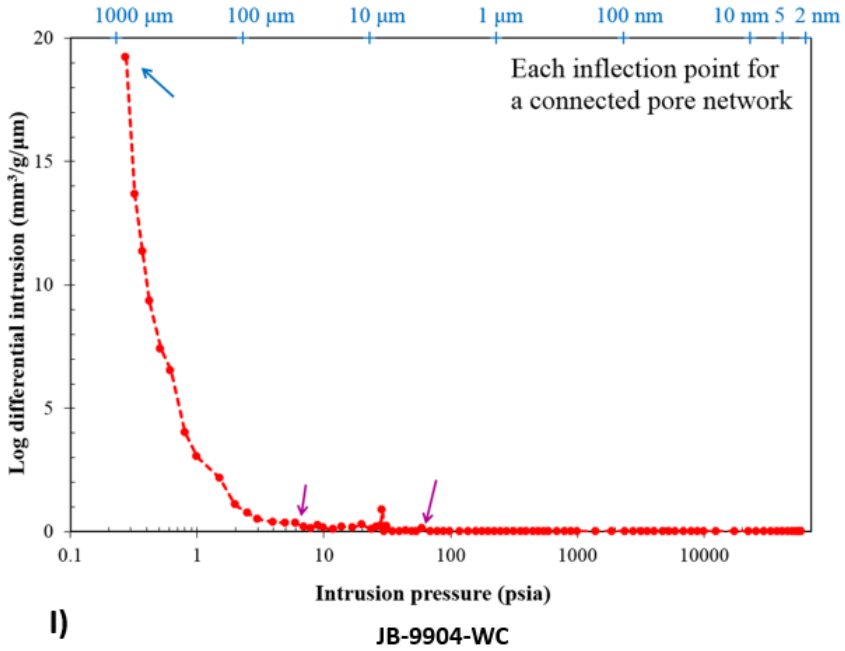

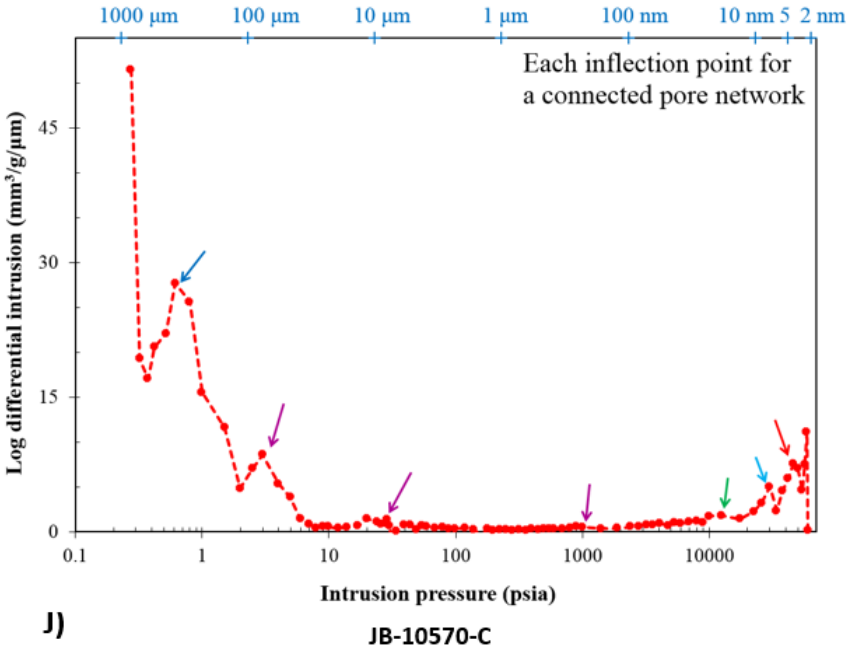

Sample ID	Bulk density (g/cm^3)	Skeletal density (g/cm^3)	Porosity (%)
W-8203-D	2.393	2.599	7.95
W-8279-D	2.435	2.650	8.12
W-8280-D	2.422	2.648	8.55
W-8291-D	2.426	2.651	8.51
W-8292-D	2.435	2.669	8.78
ME-8444-WC	2.461	2.556	3.73
ME-8455-WC	3.049	3.113	2.05
ME-8463-WC	2.345	2.457	4.56
JB-9904-WC	2.536	2.580	1.69
JB-10570-C	2.416	2.595	6.54

Table 7: Density and porosity values results from MICP analysis

Sample ID	Median pore-throat diameter (nm)		Average pore-throat diameter (nm)
	Volume	Area	
W-8203-D	19.8	7.4	15.0
W-8279-D	22.7	7.2	14.7
W-8280-D	25.9	7.2	16.0
W-8291-D	172.8	20.6	59.0
W-8292-D	174.1	21.3	67.1
ME-8444-WC	191730	4.1	12.6
ME-8455-WC	370775	40770	0
ME-8463-WC	190370	3.9	25.1
JB-9904-WC	486846	56740	0
JB-10570-C	259299	4.0	35.2

Table 8: Median and average pore throat diameter calculated from MICP analysis

Sample ID	Pore-throat diameter %									
	100-1110 µm	10-100 µm	1-10 µm	0.1-1 µm	0.05-0.1 µm	0.01-0.05 µm	0.005-0.01 µm	0.0028-0.005 µm	2.8-50 nm	>100 nm
W-8203-D	19.2	7.5	5.4	4.2	3.9	44.9	11.6	3.3	59.7	36.4
W-8279-D	8.3	10.5	4.1	7.2	8.5	46.3	10.8	4.3	61.4	30.1
W-8280-D	14.1	9.3	5.4	8.7	6.9	41.4	10.9	3.4	55.6	37.4
W-8291-D	9.2	2.4	0.2	62.9	9.8	16.8	-0.1	-1.2	15.5	74.6
W-8292-D	18.0	1.6	0.3	57.4	8.3	14.1	0.3	0.0	14.4	77.3
ME-8444-WC	53.0	3.7	2.8	1.6	1.1	8.9	17.1	11.7	37.6	61.2
ME-8455-WC	91.6	6.8	1.6	0.0	0.0	0.0	0.0	0.0	0.0	100.0
ME-8463-WC	70.0	10.2	0.4	0.5	0.3	4.4	7.4	6.8	18.7	81.0
JB-9904-WC	95.6	3.7	0.7	0.0	0.0	0.0	0.0	0.0	0.0	100.0
JB-10570-C	73.2	8.4	1.5	1.5	0.9	4.5	5.5	4.5	14.5	84.7

Table 9: Pore-throat diameter percentage determined from MICP analysis. Represents the percentage that each pore-throat region contributes towards the total pore network.

Sample ID	Predominant (>100 nm) pore-throat network		Predominant (2.8-50 nm) pore-throat network		Gao and Hu Permeability k_{GH} (mD)
	Permeability k_{100} (mD)	Effective tortuosity	Permeability $k_{2.8\text{-}50}$ (mD)	Effective tortuosity	
W-8203-D	3.17E+02	18.9	5.93E-05	39742	5.72E-05
W-8279-D	1.92E+01	45.6	7.41E-05	23181	1.22E-04
W-8280-D	1.99E+01	48.1	5.62E-05	28590	1.04E-04
W-8291-D	6.74E-02	789.2	7.35E-04	7561	7.13E-03
W-8292-D	4.82E-01	483.4	1.14E-04	29981	7.26E-03
ME-8444-WC	8.61E+03	4.3	8.24E-06	138798	4.26E+04
ME-8455-WC	1.12E+04	3.2	-	-	1.85E+05
ME-8463-WC	4.79E+03	4.7	1.10E-05	116605	4.19E+04
JB-9904-WC	2.07E+04	2.5	-	-	3.38E+05
JB-10570-C	1.51E+04	4.3	1.33E-05	145123	8.33E+04

Table 10: Dual pore-throat networks permeability and tortuosity calculated from MICP analysis

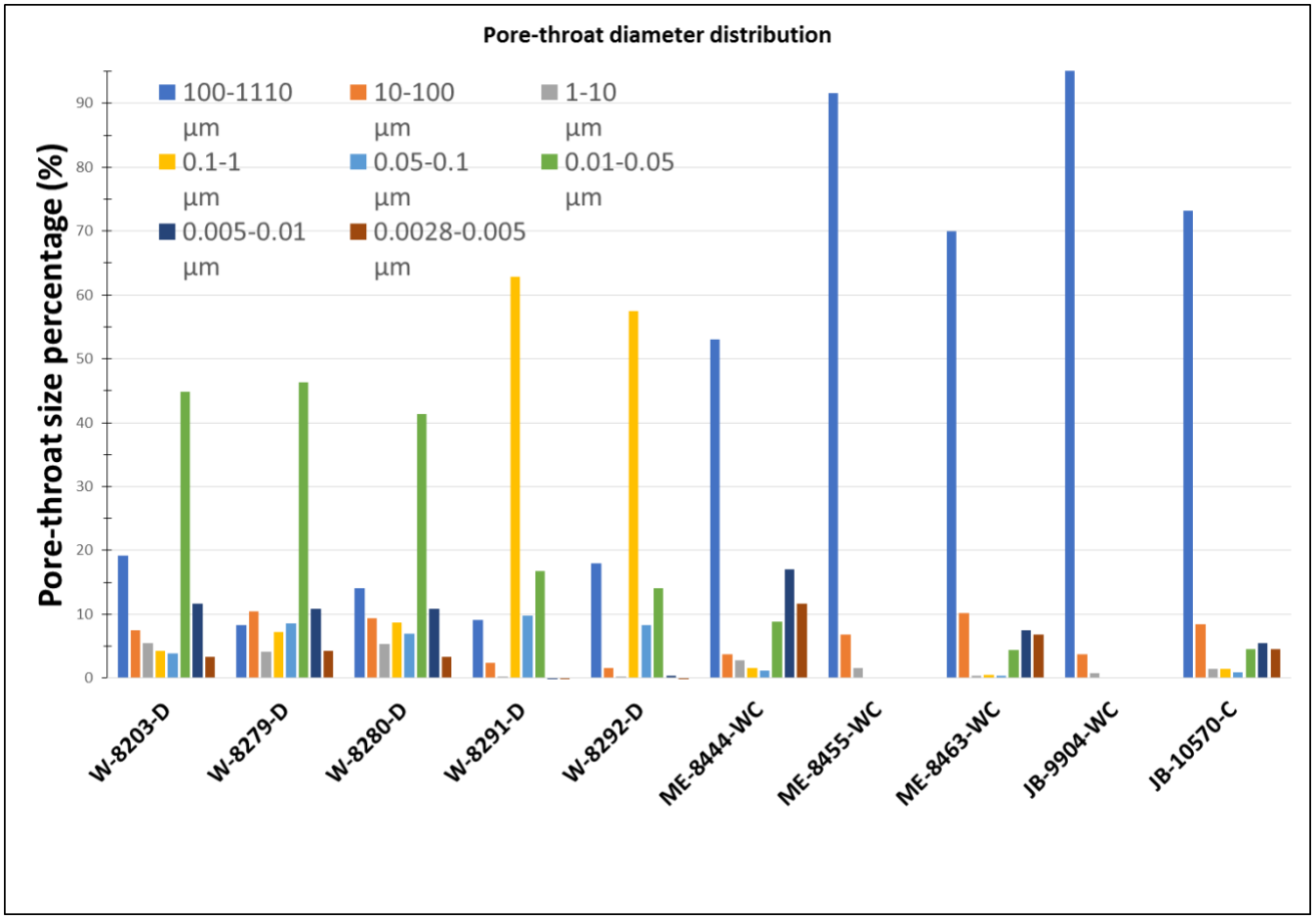

Figure 19: Histogram of the pore-throat diameter distribution determined by MICP analysis.

Sample ID	"Matrix" region (<50 µm) (%)	"Fracture" region (>50 µm) (%)
ME-8444-WC	1.748	1.981
ME-8455-WC	0.072	1.980
ME-8463-WC	1.040	3.519
JB-9904-WC	0.045	1.643
JB-10570-C	1.410	5.126

Table 11: Porosity calculated using two separate regions (>50 µm and <50 µm) during MICP processing

Wettability and contact angle

By analyzing successive time-stamped images, the angle of fluid droplets interacting with the sample surface with respect to time was determined. Figure 20 illustrates the process of measuring contact angles from images. Figure 21 shows the contact angle measurement for each fluid in log time. Only samples W-8203-D, W-8279-D, W-8280-D, W-8291-D, W-8292-D, and ME-8444-D were tested for contact angle due to sample mass limitations. Fifteen seconds after the droplet makes contact with the sample surface, the contact angle was recorded and noted in Table 12. For n-decane droplets, the contact angle was immediately recorded instead of at 15 seconds after contact due to nearly instantaneous spreading over the surface. The detection limit of the device was 1.5°. Whenever the contact angle was below the detection limit (i.e. 1.5°), the measurement at that time was approximated at 1.5°.

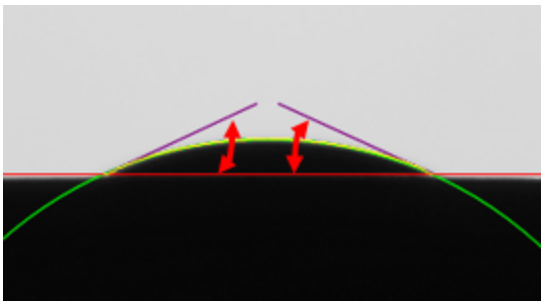

Figure 20: DI water contact angle measurement for W-8203-D. Imaging records the spreading of the fluid droplet across the sample surface through time. The interaction of the droplet is an indication of the samples wettability. Red arrows indicate the angle being measured.

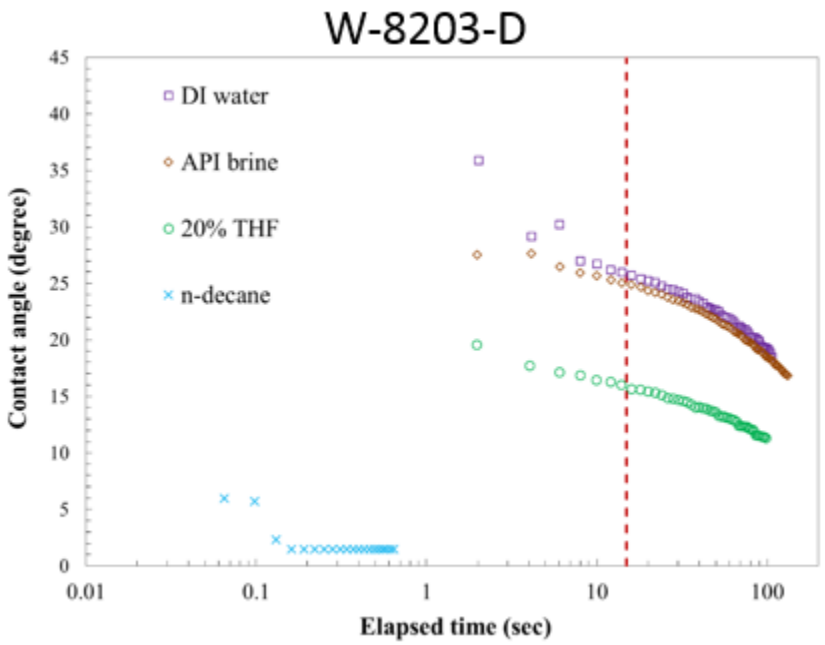

Figure 21: Fluid droplet contact angle with W-8203-D. Performed using DI water, API brine, 20% THF mixed in water, and n-decane

Figure 21 (cont.):

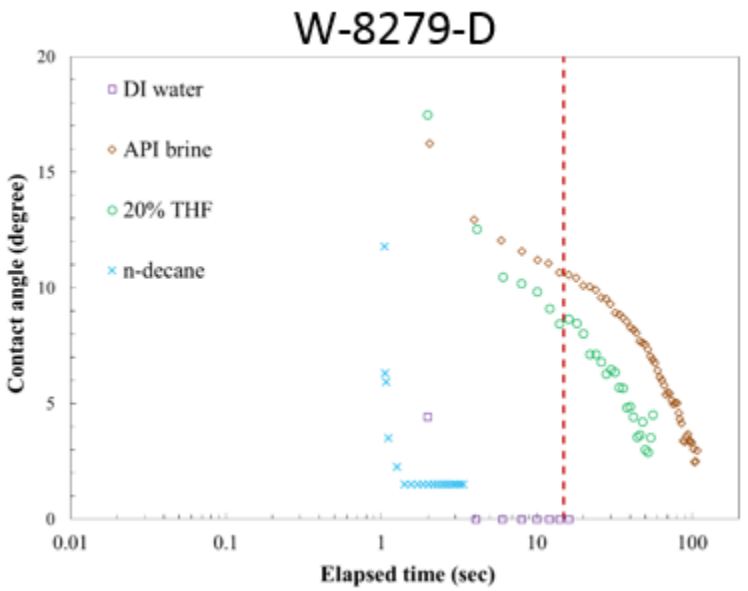

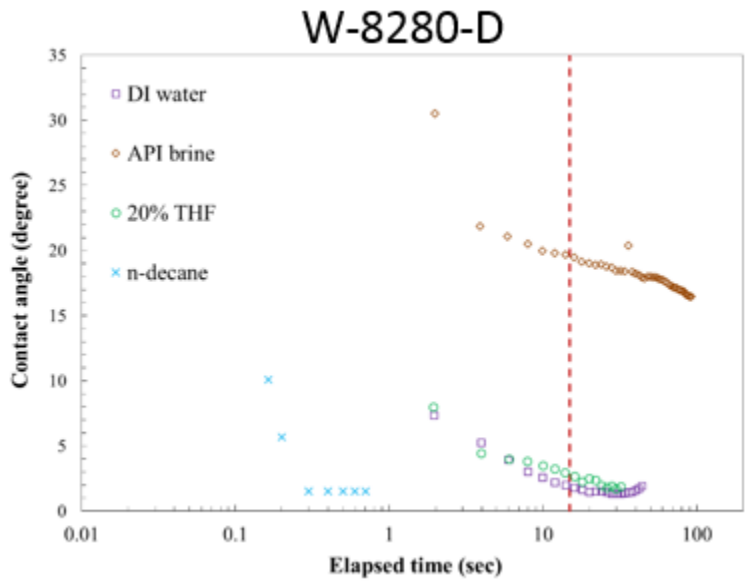

Figure 21 (cont.):

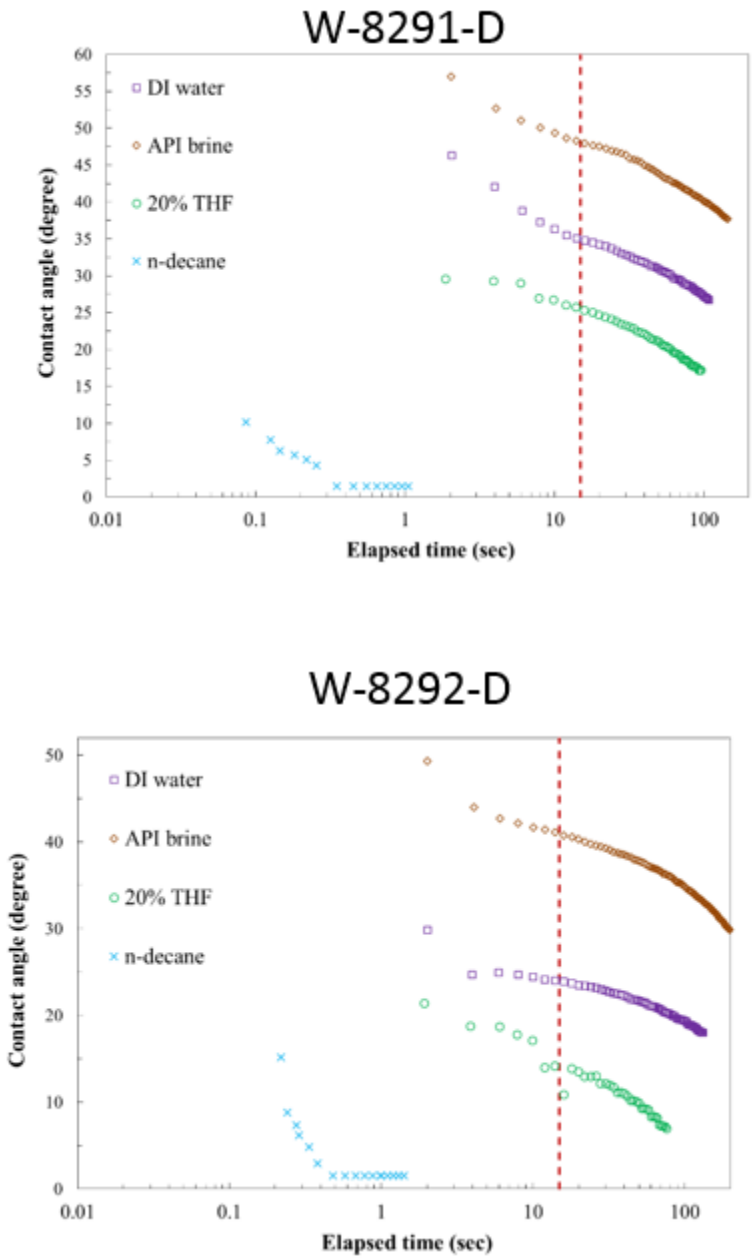

Figure 21 (cont.):

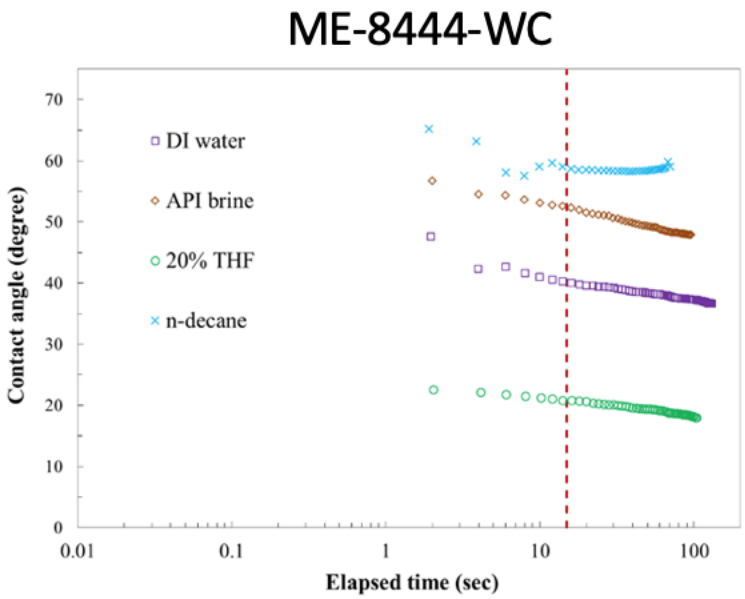

Sample ID	Contact Angle (°)			
	DIW	API Brine	THF	n-decane
W-8203-D	24.1	23.3	14.6	9.0 - 1.5
W-8279-D	1.5-4.4	8.9	6.4	11.7 - 1.5
W-8280-D	1.5	18.4	1.9	10.1 - 1.5
W-8291-D	32.6	45.9	23.1	10.1 - 1.5
W-8292-D	22.7	39.3	12.0	15.1 - 1.5
ME-8444-WC	39.1	51.2	20.0	65.2 - 58.3

Table 12: Fluid contact angle measurements, recorded 15 seconds after initial contact. N-decane measurement range consists of the contact angle immediately at contact to the detection limit of the device (1.5°)

Vacuum saturation

A summary of the results obtained from DIW, DT2, and THF vacuum saturation experiments are provided in Table 13. Sample slabs were tested with DIW vacuum saturation only. DIW vacuum saturation was performed on three different 1 cm^3 cubes. The average porosity, bulk density, and grain density from the three separate cubes are presented in Table 7. One cube for each sample was used to determine porosity, bulk density, and grain density using DT2 and THF vacuum saturation tests.

The Dean samples exhibit significantly higher porosity than the Wolfcamp and Canyon samples. Porosity values calculated using DIW, THF, and DT2 show a marked difference. Generally, the porosity values calculated using THF are the lowest while porosity calculated using DIW and DT2 are the highest.

Sample ID	Slab (~4 cm across)			Cubes (1 cm^3)								
	DI Water			DI Water			DT2			THF		
	Porosity (%)	Bulk Density (g/cc)	Grain Density (g/cc)	Porosity (%)	Bulk Density (g/cc)	Grain Density (g/cc)	Porosity (%)	Bulk Density (g/cc)	Grain Density (g/cc)	Porosity (%)	Bulk Density (g/cc)	Grain Density (g/cc)
W-8203-D	7.439	2.341	2.530	7.538 ± 0.120	2.428 ± 0.007	2.626 ± 0.010	8.155	2.346	2.555	8.497	2.617	2.860
W-8279-D	8.004	2.466	2.681	11.209 ± 1.244	2.427 ± 0.008	2.734 ± 0.043	8.808	2.438	2.673	7.414	1.955	2.111
W-8280-D	9.021	2.339	2.571	9.646 ± 0.017	2.391 ± 0.015	2.646 ± 0.017	9.597	2.456	2.716	8.567	2.345	2.565
W-8291-D	7.146	2.461	2.651	10.399 ± 2.54	2.437 ± 0.021	2.722 ± 0.088	9.093	2.494	2.743	7.000	2.459	2.644
W-8292-D	6.25	2.462	2.626	9.600 ± 2.609	2.443 ± 0.054	2.704 ± 0.111	8.357	2.465	2.690	7.155	2.390	2.574
ME-8444-WC				0.895 ± 0.198	2.462 ± 0.020	2.485 ± 0.015	2.063	2.474	2.526	0.792	2.515	2.535
ME-8455-WC				0.846 ± 0.443	2.595 ± 0.002	2.617 ± 0.014	1.673	2.599	2.643	0.399	2.431	2.441
ME-8463-WC				1.485 ± 0.646	2.531 ± 0.014	2.569 ± 0.021	2.114	2.502	2.556	1.338	2.470	2.503
JB-9904-WC				3.027 ± 2.997	2.582 ± 0.007	2.671 ± 0.085	1.188	2.588	2.619	0.027	2.549	2.549
JB-10570-C				2.667 ± 0.139	2.561 ± 0.019	2.631 ± 0.023	2.195	2.57	2.627	2.552	2.450	2.514

Table 13: Calculated porosity, bulk density, and grain density values for test samples from DI water, DT2, and THF fluid vacuum saturation tests.

Fluid imbibition

Spontaneous fluid imbibition tests were performed using both DIW and DT2 fluid. Broadly, four slope regions are identified when plotting cumulative imbibition versus time in log-log space for DIW. Only three distinct regions are identified for DT2 tests.

In the first minute, the logarithm of cumulative imbibition versus time ranges exhibits a slope of 2-4. These early slopes, termed Type I, are associated with the initial fluid surface and sample interaction. If microfractures or laminations are present in the sample, this initial slope region will be followed by a period of prolonged, relatively high fluid imbibition. These Type II slopes are typically around 2/3 and can possibly persist up to one or two hours. Type III, the connectivity slope, is the slope region that is illustrative of the pore throat network of the sample. The Type III region exhibits slopes from 0.25-0.5, depending on how connected the fluid pathways of the sample are. A higher slope III is indicative of a more connected sample. The results from both DIW and DT2 tests are provided in Figure 22. The red line in Figure 22 was interpreted as the connectivity slope. Near the end of the tests when the pore space of the sample was fully saturated, the imbibition slope flattened to ~0.1. This Type IV slope region was a result of the imbibing fluid reaching the top of the sample. Table 14 provides the connectivity slope values for each sample.

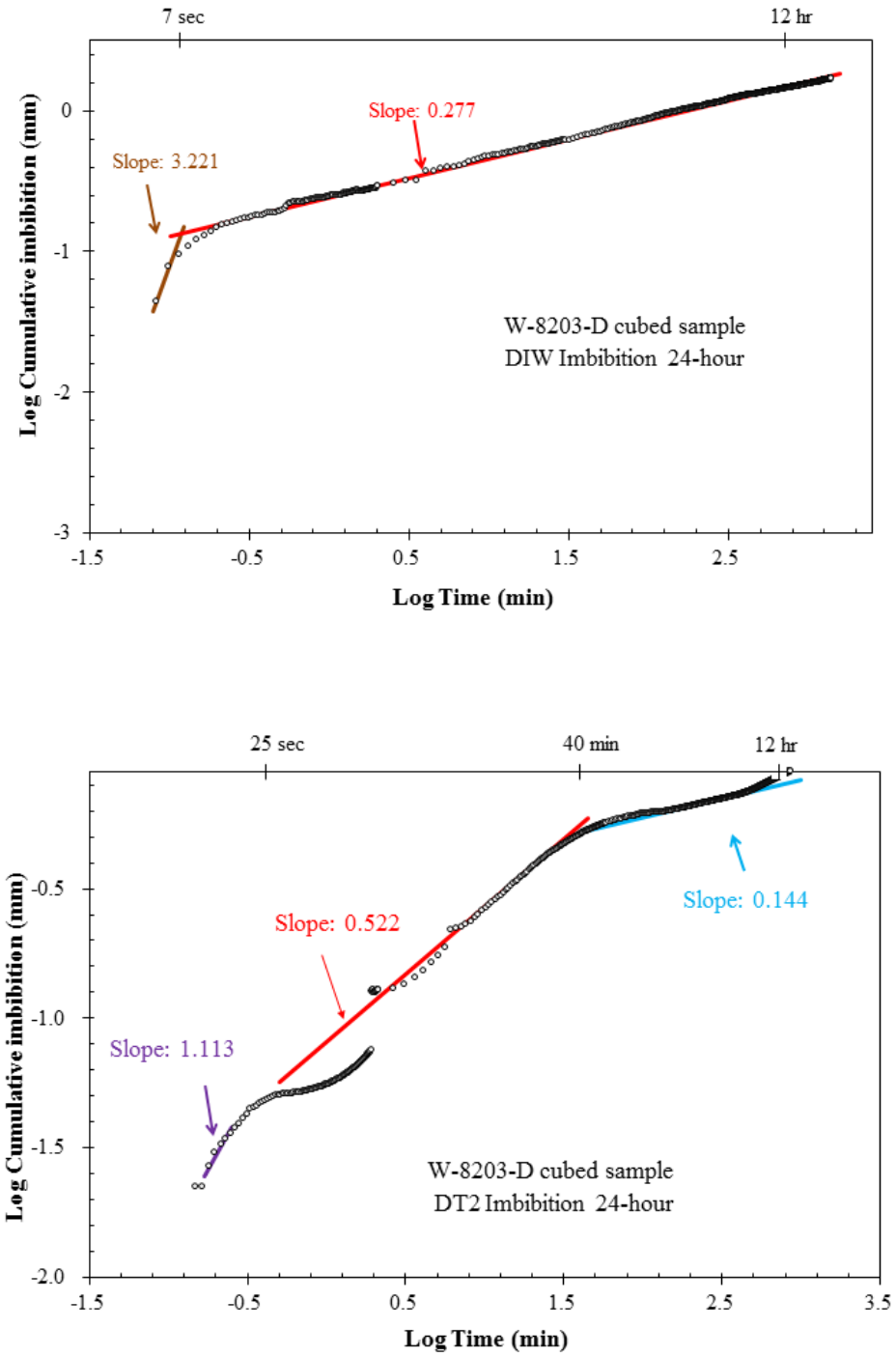

Figure 22: Imbibition slopes observed during spontaneous fluid imbibition with either DIW (top) or DT2 (bottom).

Figure 22 (cont.):

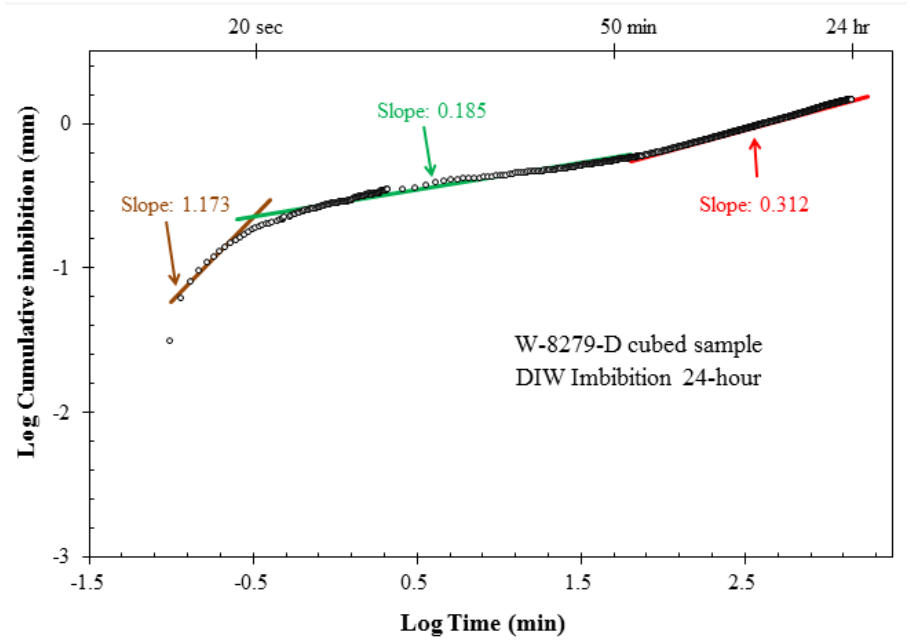

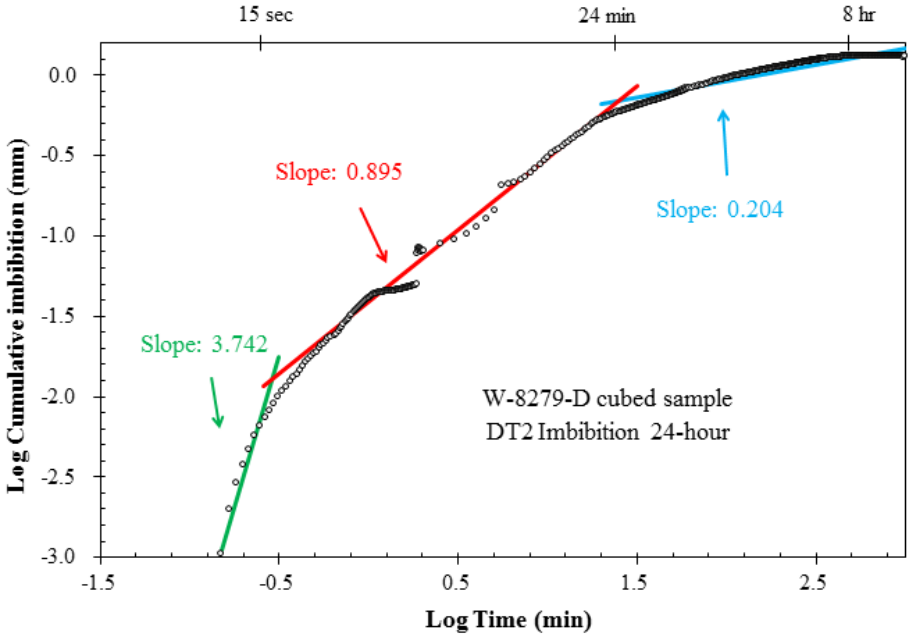

Figure 22 (cont.):

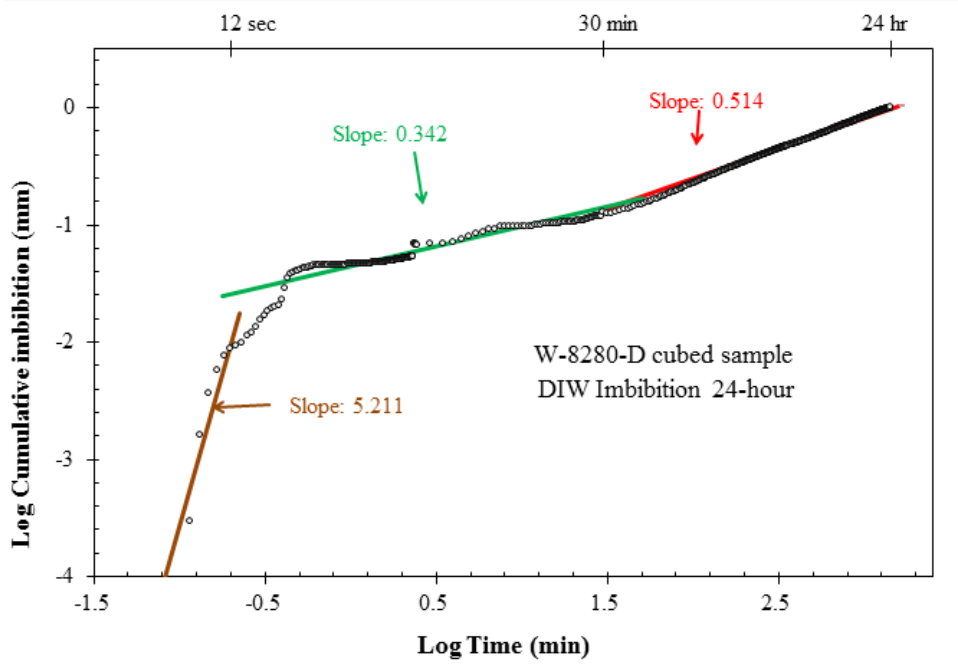

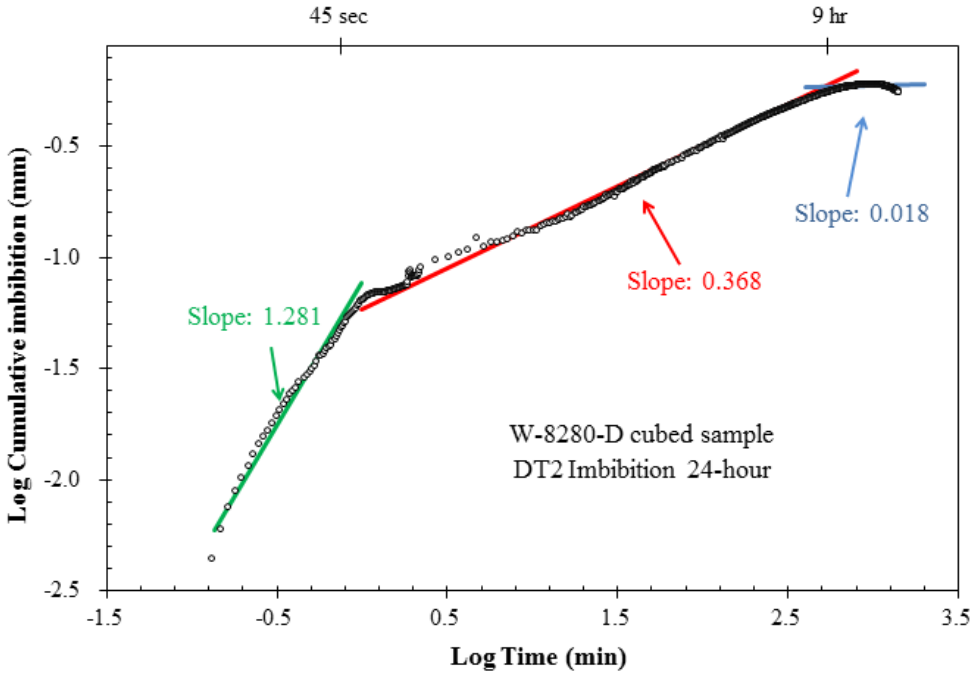

Figure 22 (cont.):

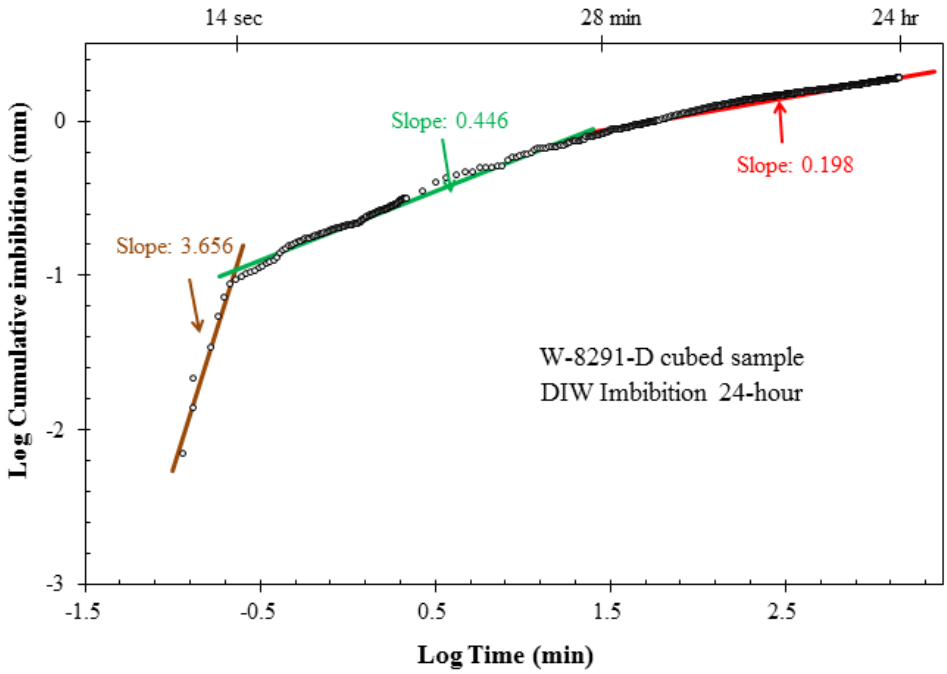

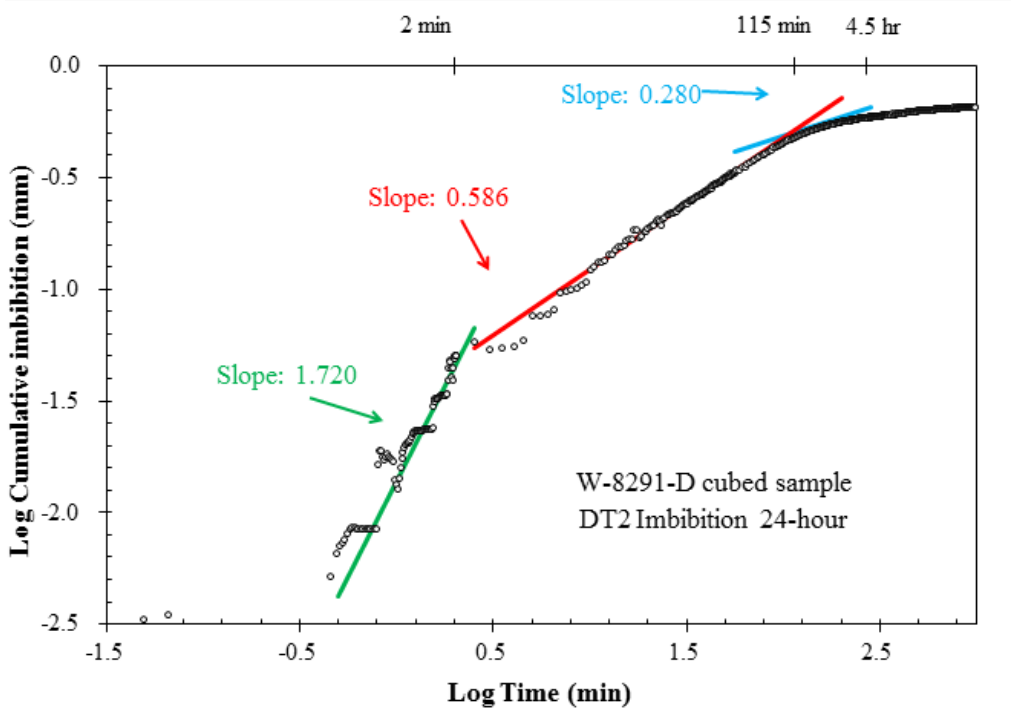

Figure 22 (cont.):

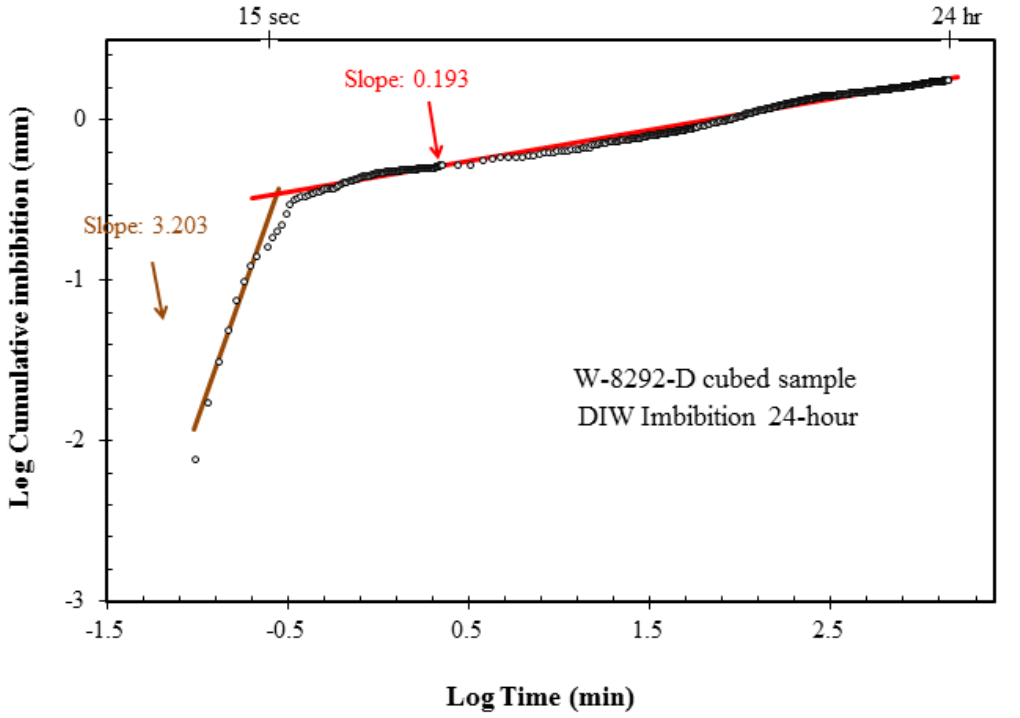

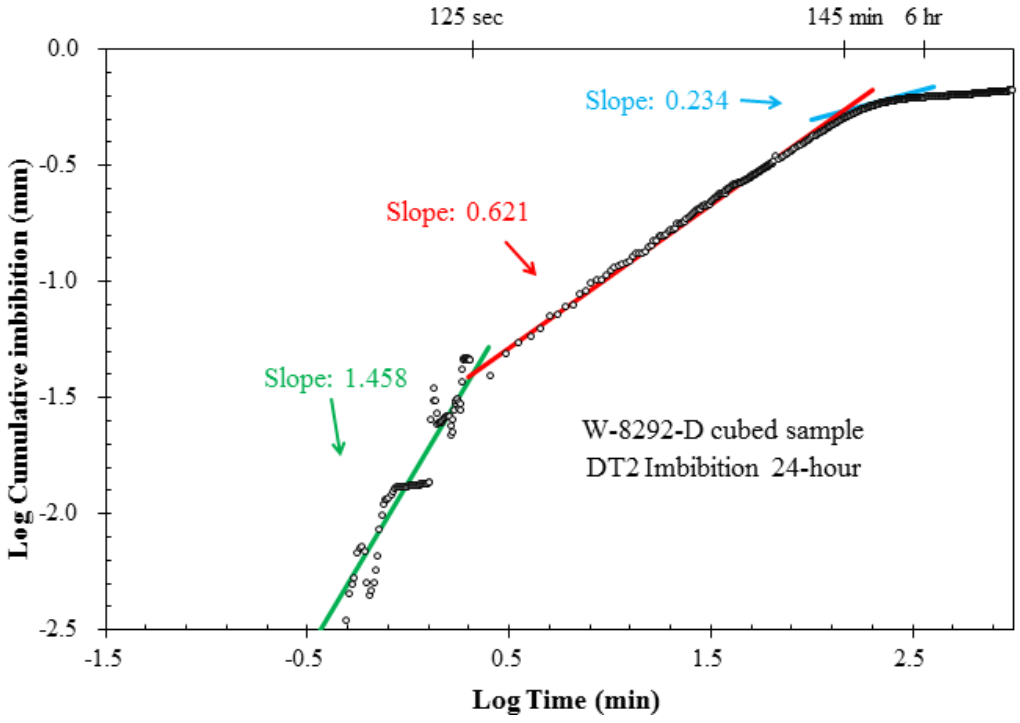

Figure 22 (cont.):

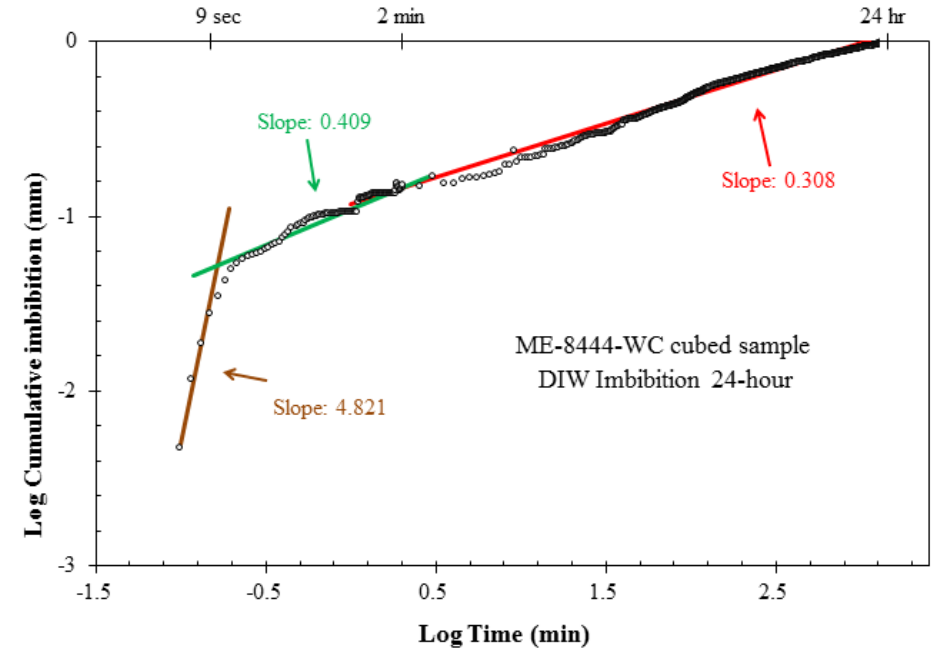

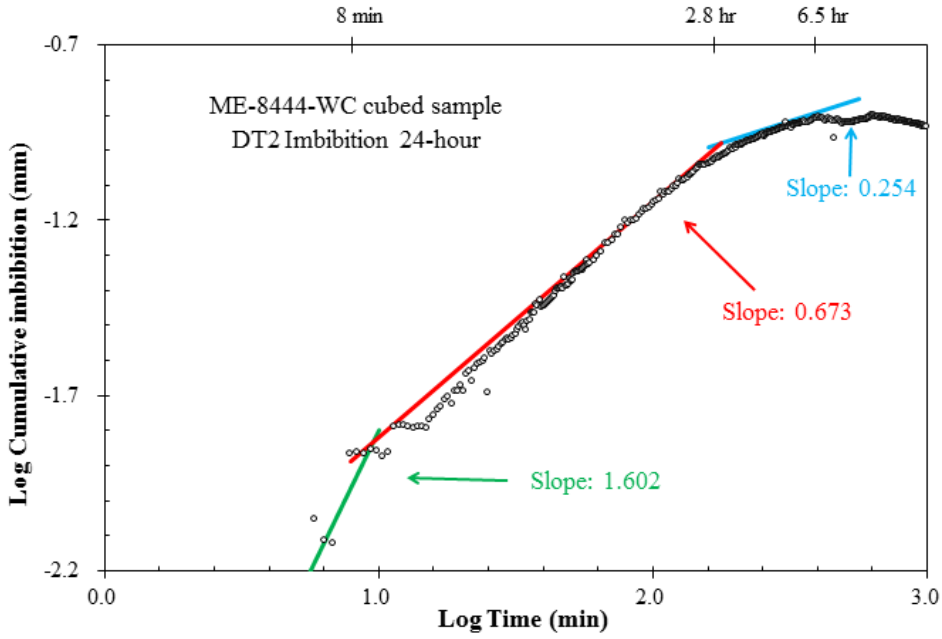

Figure 22 (cont.):

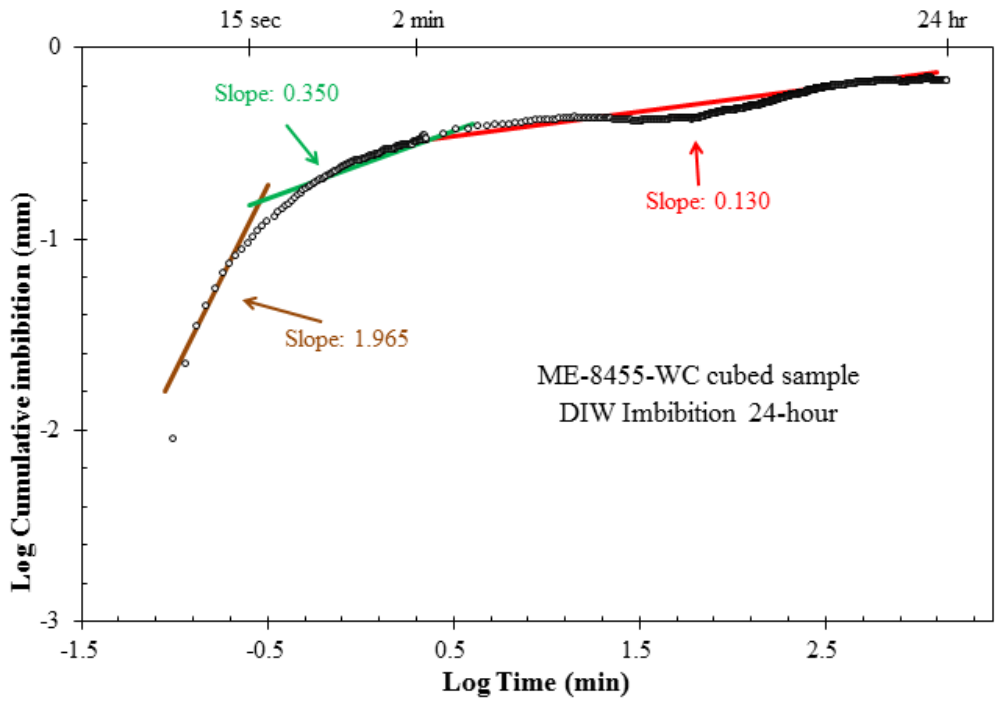

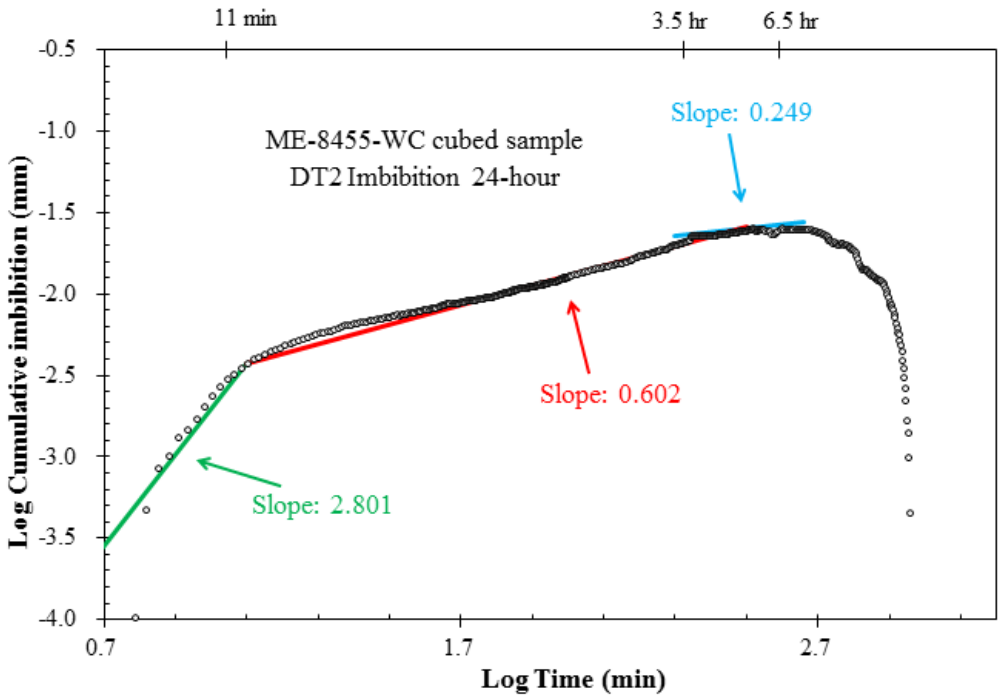

Figure 22 (cont.):

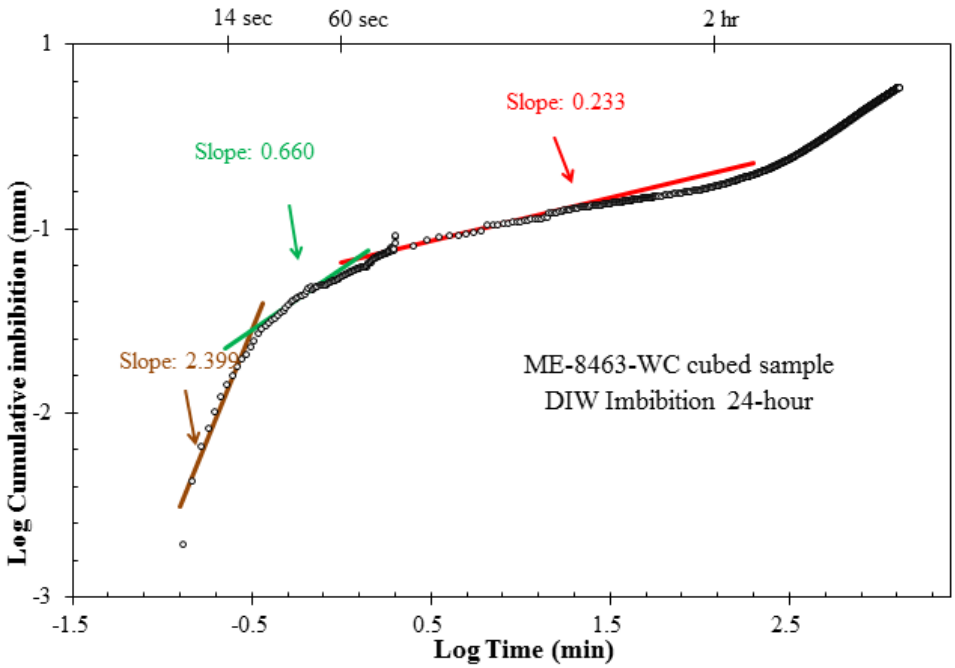

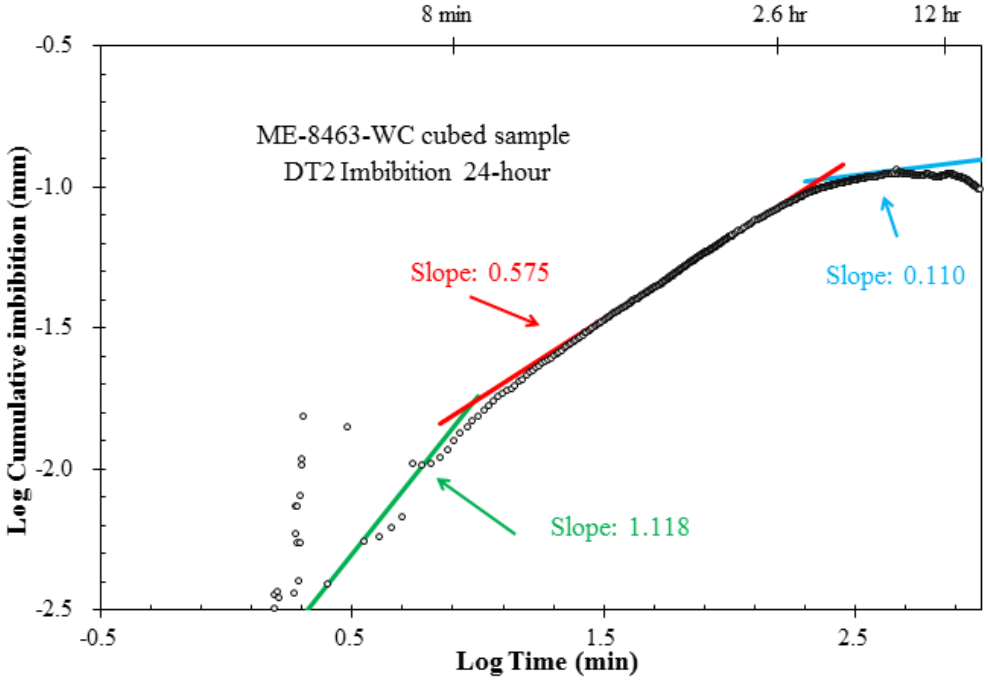

Figure 22 (cont.):

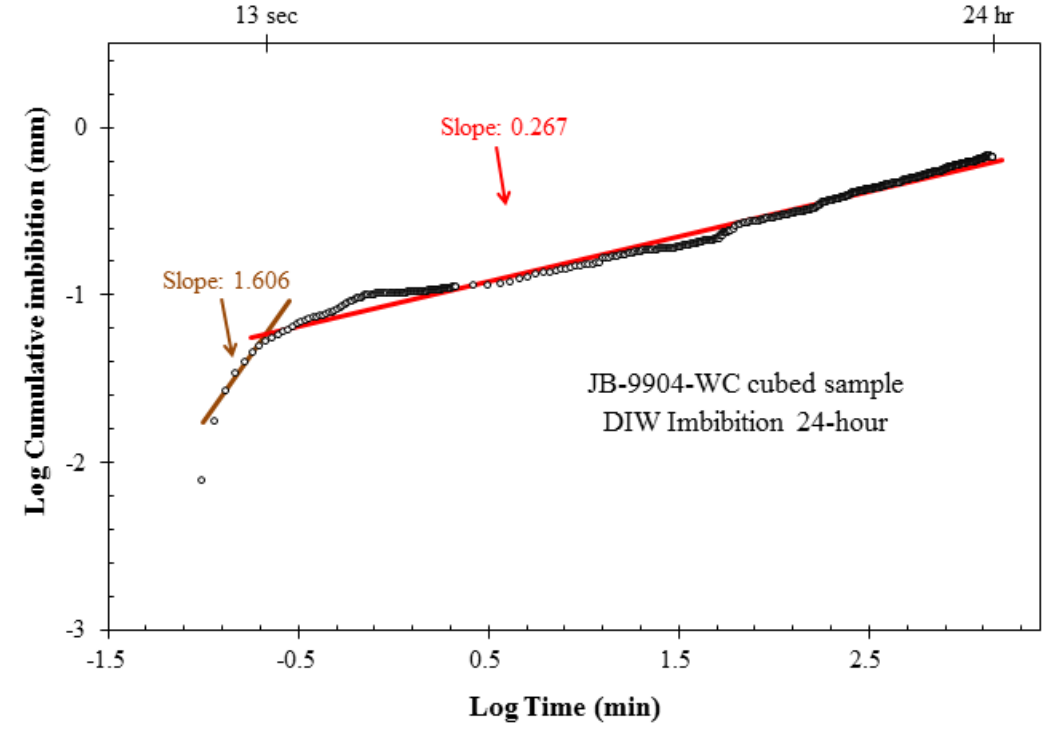

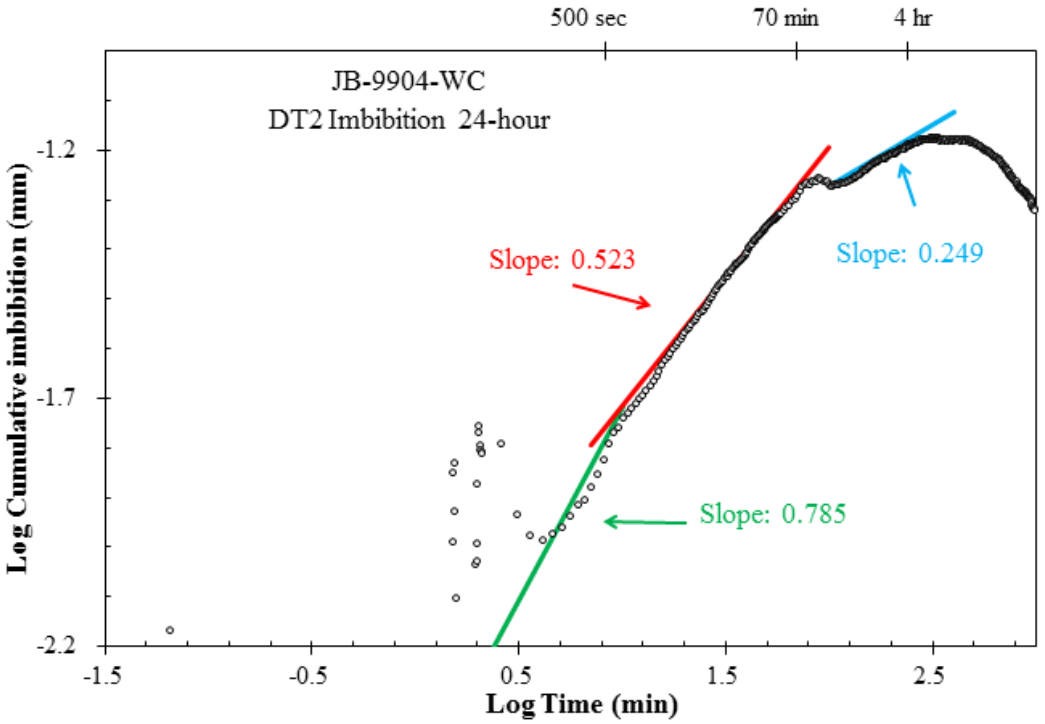

Figure 22 (cont.):

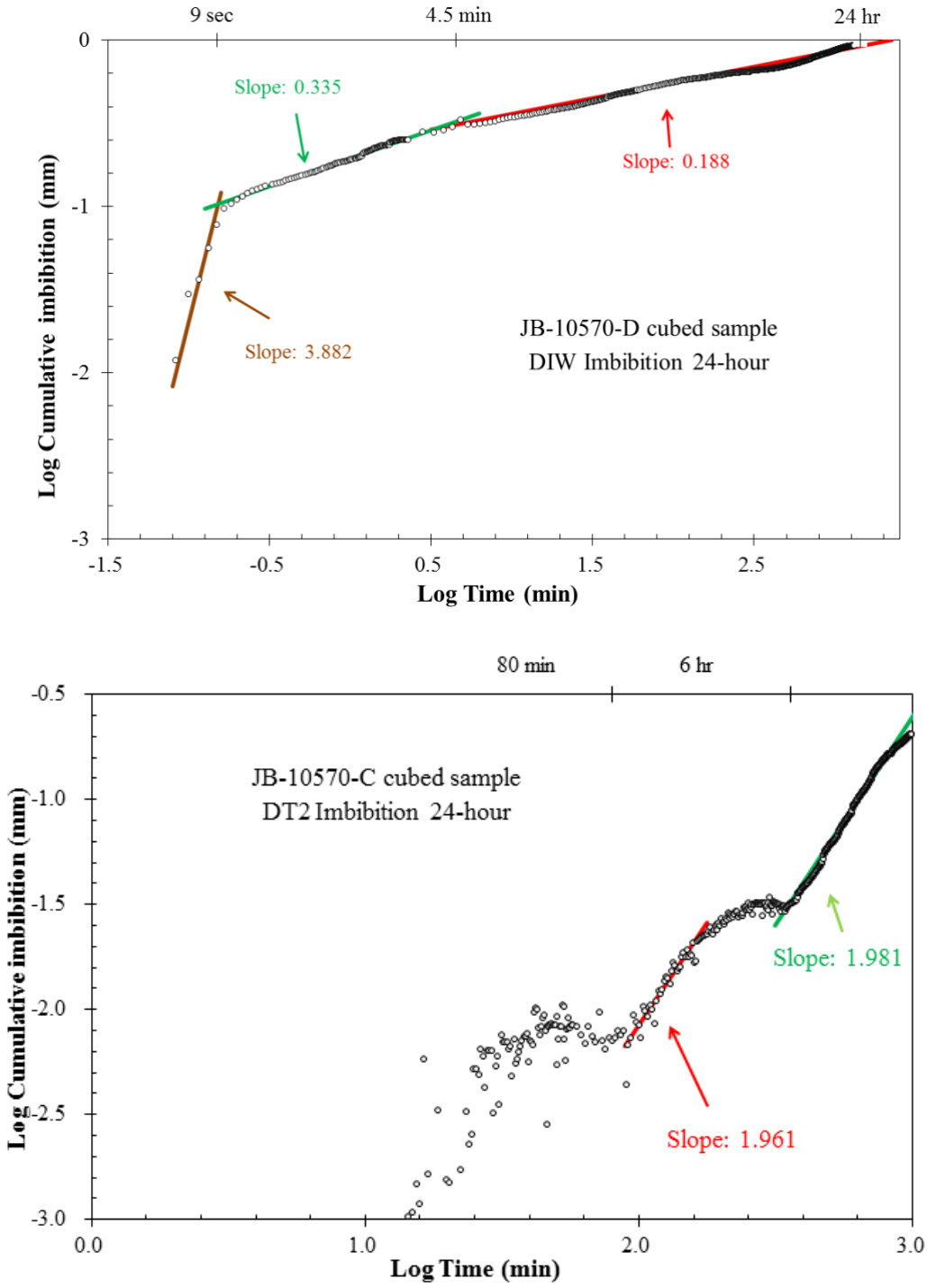

Sample ID	Connectivity Slope	
	DIW	DT2
W-8203-D	0.277	0.581
W-8279-D	0.312	0.895
W-8280-D	0.514	0.368
W-8291-D	0.198	0.586
W-8292-D	0.193	0.621
ME-8444-WC	0.308	0.673
ME-8455-WC	0.130	0.602
ME-8463-WC	0.233	0.575
JB-9904-WC	0.267	0.249
JB-10570-C	0.188	1.961

Table 14: Spontaneous imbibition connectivity slopes observed when plotting cumulative imbibition vs. time in log-log space.

Liquid pycnometry

Density measurements from liquid pycnometry are presented in Table 15. Liquid pycnometry measurements are limited by the sample mass available. Ideally, a greater grain size range would be tested in order to better assess edge-accessible porosity. Cubes, GRI, Size B, Size, and C each included three DIW trials to determine apparent bulk density. Only one DIW trial was performed on slab samples. Two trials for each DT2 and THF fluids were completed for GRI, Size B, and Size C sample powder. Apparent bulk density measurements for cubes using THF and DT2 fluids includes one trial each.

Apparent bulk density generally decreased when calculated with either DT2 or THF relative to the apparent bulk density calculated using DIW. Apparent bulk density values

determined using THF exhibit the highest variation while DIW results are more consistent across sample types. Figure 23 illustrates apparent bulk density variations across fluids and sample types.

Sample ID	Size designation	Size	Size	Equivalent spherical diameter (µm)	DIW	THF	DT2
					Apparent bulk density (g/cm^3)		
W-8203-D	Irregular	Irregular	~4.0 cm across	70105	2.341		
	Cube	Cube (1 cm side)	Cube (1 cm side)	6204	2.428 ± 0.007	2.617	2.346
	GRI	Mesh -20/+35	500 - 841 µm	671	2.554 ± 0.030	2.380 ± 0.150	2.507 ± 0.039
	Size B	Mesh -35/+80	177 - 500 µm	339	2.545 ± 0.030	2.512 ± 0.030	2.589 ± 0.038
	Size C	Mesh -80/+200	75 - 177 µm	126	2.378 ± 0.017	2.299 ± 0.073	2.349 ± 0.015
W-8279-D	Irregular	Irregular	~4.0 cm across	70105	2.466		
	Cube	Cube (1 cm side)	Cube (1 cm side)	6204	2.427 ± 0.008	1.955	2.438
	GRI	Mesh -20/+35	500 - 841 µm	671	2.626 ± 0.007	2.614 ± 0.044	2.548 ± 0.060
	Size B	Mesh -35/+80	177 - 500 µm	339	2.579 ± 0.036	2.262 ± 0.327	2.530 ± 0.035
	Size C	Mesh -80/+200	75 - 177 µm	126	2.355 ± 0.045	2.699 ± 0.148	2.445 ± 0.085
ME-8444-WC	Irregular	Irregular	~4.0 cm across				
	Cube	Cube (1 cm side)	Cube (1 cm side)	6204	2.462 ± 0.020	2.532	2.474
	GRI	Mesh -20/+35	500 - 841 µm	671	2.483 ± 0.011	2.690 ± 0.040	2.475 ± 0.015
	Size B	Mesh -35/+80	177 - 500 µm	339	2.508 ± 0.005	2.388 ± 0.160	2.440 ± 0.087
	Size C	Mesh -80/+200	75 - 177 µm	126	2.460 ± 0.002	2.316 ± 0.158	2.574 ± 0.022
ME-8455-WC	Irregular	Irregular	~4.0 cm across				
	Cube	Cube (1 cm side)	Cube (1 cm side)	6204	2.595 ± 0.002	2.431	2.599
	GRI	Mesh -20/+35	500 - 841 µm	671	2.583 ± 0.031	2.522 ± 0.210	2.619 ± 0.019
	Size B	Mesh -35/+80	177 - 500 µm	339	2.589 ± 0.006	2.182 ± 0.284	2.581 ± 0.008
	Size C	Mesh -80/+200	75 - 177 µm	126	2.634 ± 0.025	2.063 ± 0.214	2.612 ± 0.020
ME-8463-WC	Irregular	Irregular	~4.0 cm across				
	Cube	Cube (1 cm side)	Cube (1 cm side)	6204	2.530 ± 0.014	2.470	2.502
	GRI	Mesh -20/+35	500 - 841 µm	671	2.508 ± 0.016	2.575 ± 0.038	2.495 ± 0.006
	Size B	Mesh -35/+80	177 - 500 µm	339	2.444 ± 0.084	2.595 ± 0.046	2.419 ± 0.013
	Size C	Mesh -80/+200	75 - 177 µm	126	2.040 ± 0.099	2.298 ± 0.073	2.542 ± 0.108
JB-10570-C	Irregular	Irregular	~4.0 cm across				
	Cube	Cube (1 cm side)	Cube (1 cm side)	6204	2.561 ± 0.019	2.450	2.570
	GRI	Mesh -20/+35	500 - 841 µm	671	2.511 ± 0.021	2.383 ± 0.616	2.493 ± 0.062
	Size B	Mesh -35/+80	177 - 500 µm	339	2.503 ± 0.017	2.473 ± 0.160	2.499 ± 0.015
	Size C	Mesh -80/+200	75 - 177 µm	126	2.335 ± 0.029	2.495 ± 0.102	2.383 ± 0.014

Table 15: Apparent bulk density values determined using liquid pycnometry

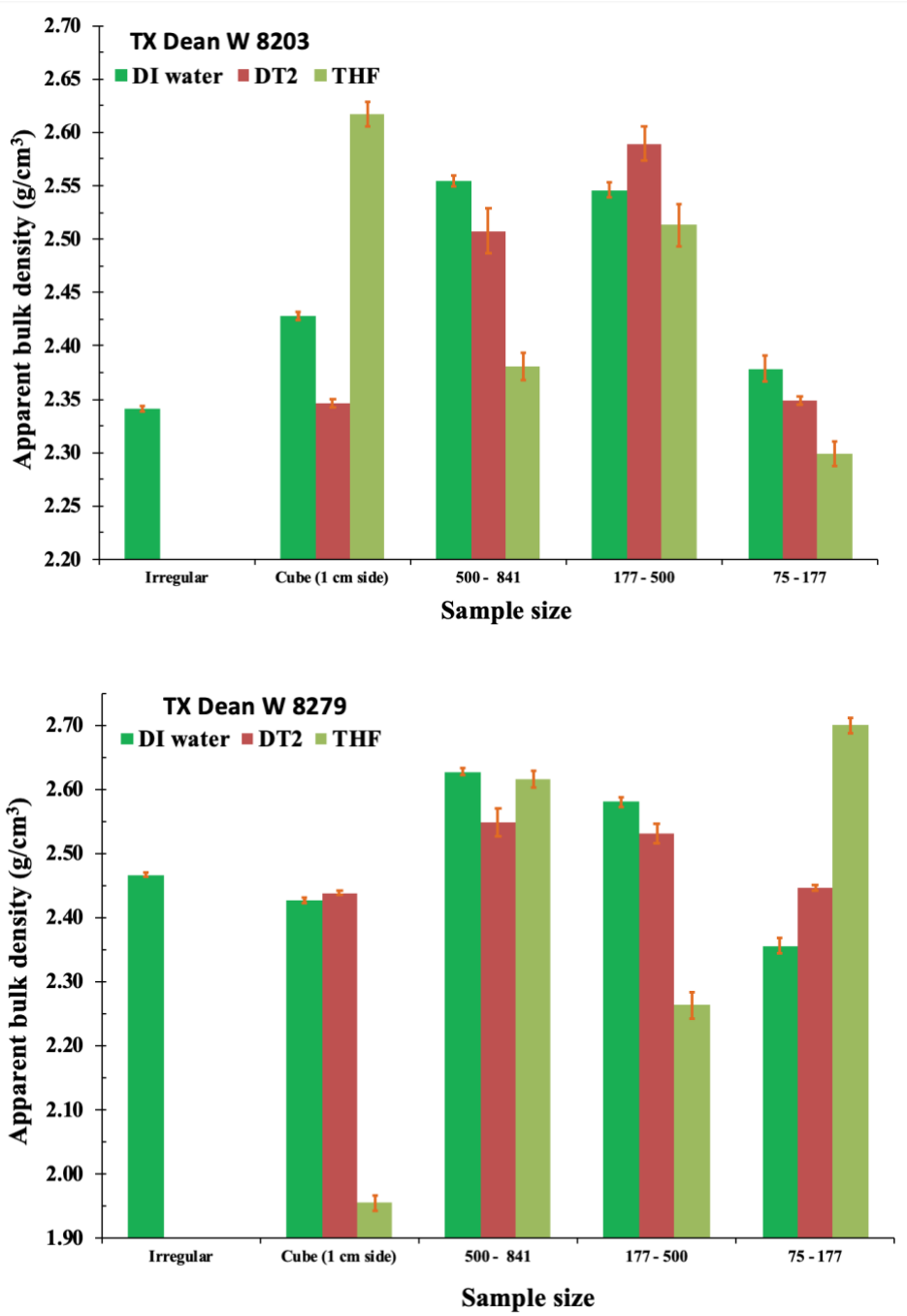

Figure 23: Apparent bulk density variation between DIW, DT2, and THF liquid pycnometry testing

Figure 23 (cont.):

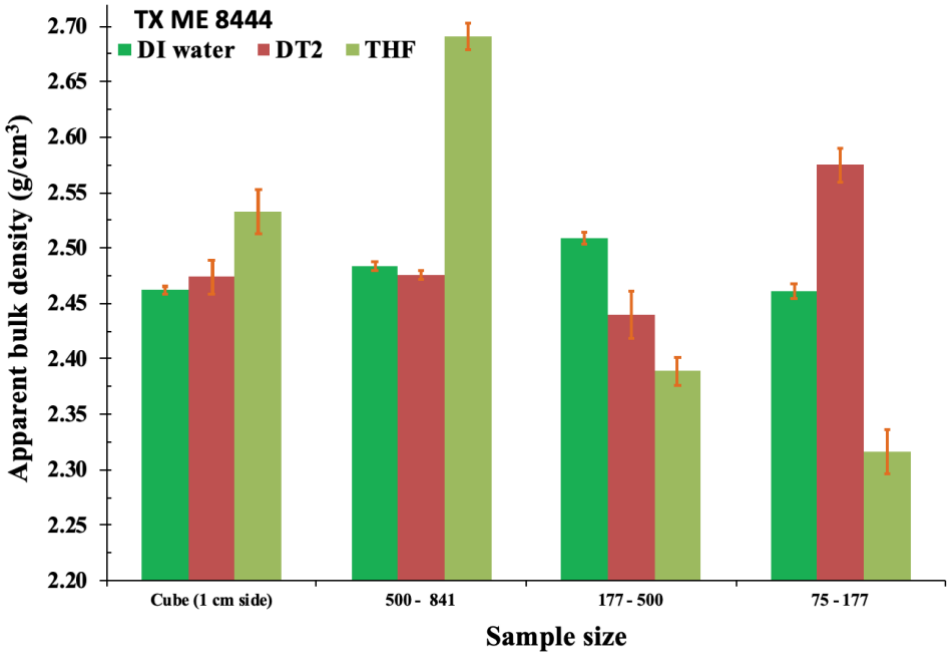

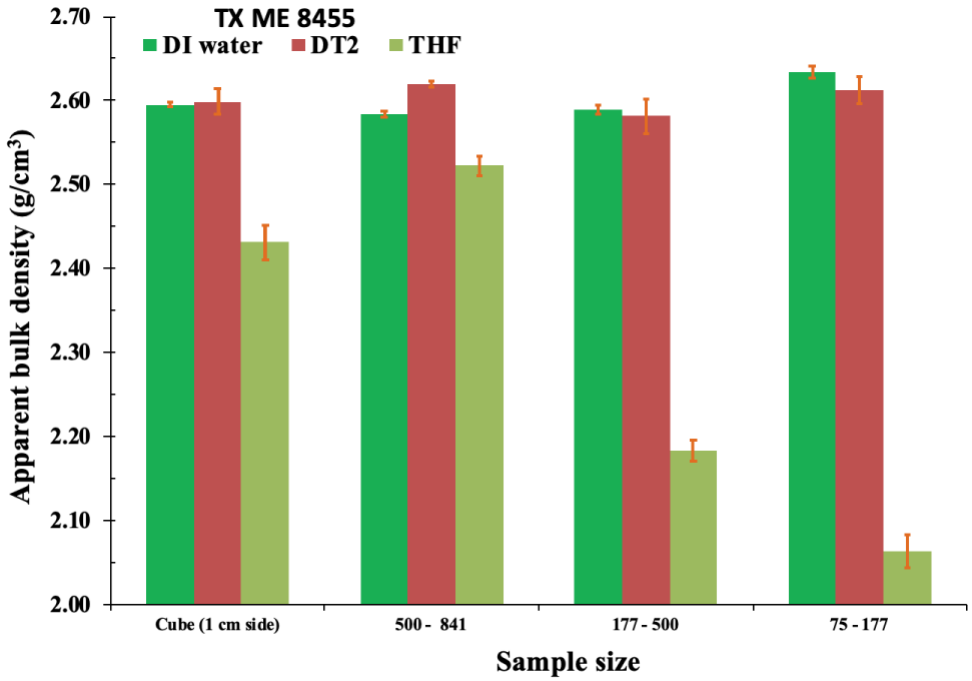

Figure 23 (cont.):

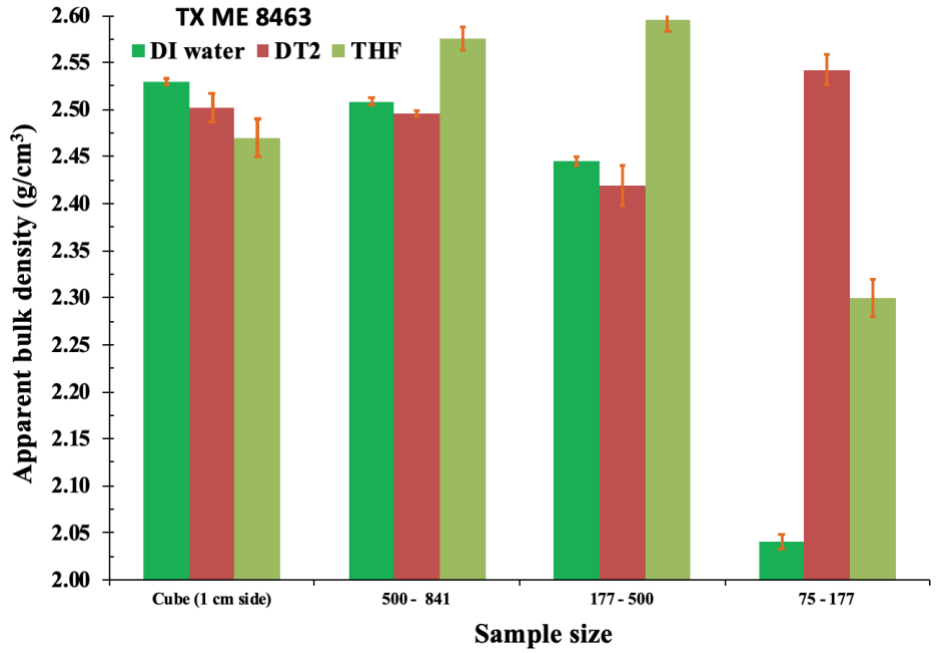

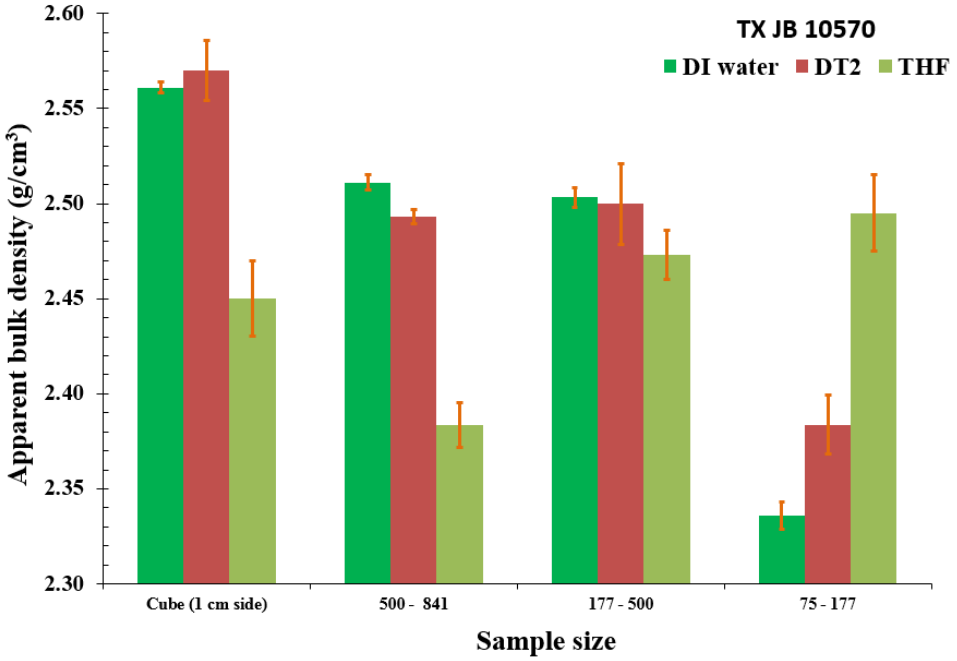

DISCUSSION

Pore structure, minerology and geochemistry

Pore structure of a porous media is influenced by combination of mineralogical and geochemical effects. The three formations studied each have unique mineralogy, geochemistry, and diagenetic history, which shape their pore structure.

Fishman et al. (2013) showed in Eagle Ford samples that organic pore space is better-developed with higher thermal maturity values (R_{oe}). Additionally, a positive relationship between overall porosity and TOC has been noted by examination of dozens of shale formations worldwide (Passey et al., 2010). Wolfcamp samples tested here are high in TOC and low in porosity. There appears to be a weak, positive trend between TOC and porosity in the Wolfcamp (Figure 24). It is possible that despite high TOC in the Wolfcamp, pore space created by the maturation of kerogen (i.e. organic porosity) was outweighed by pore space destruction through diagenetic processes. The filling of pores by carbonate cementation has been noted in the Wolfcamp formation (Wickhard Elmore and Gerhard, 2016).

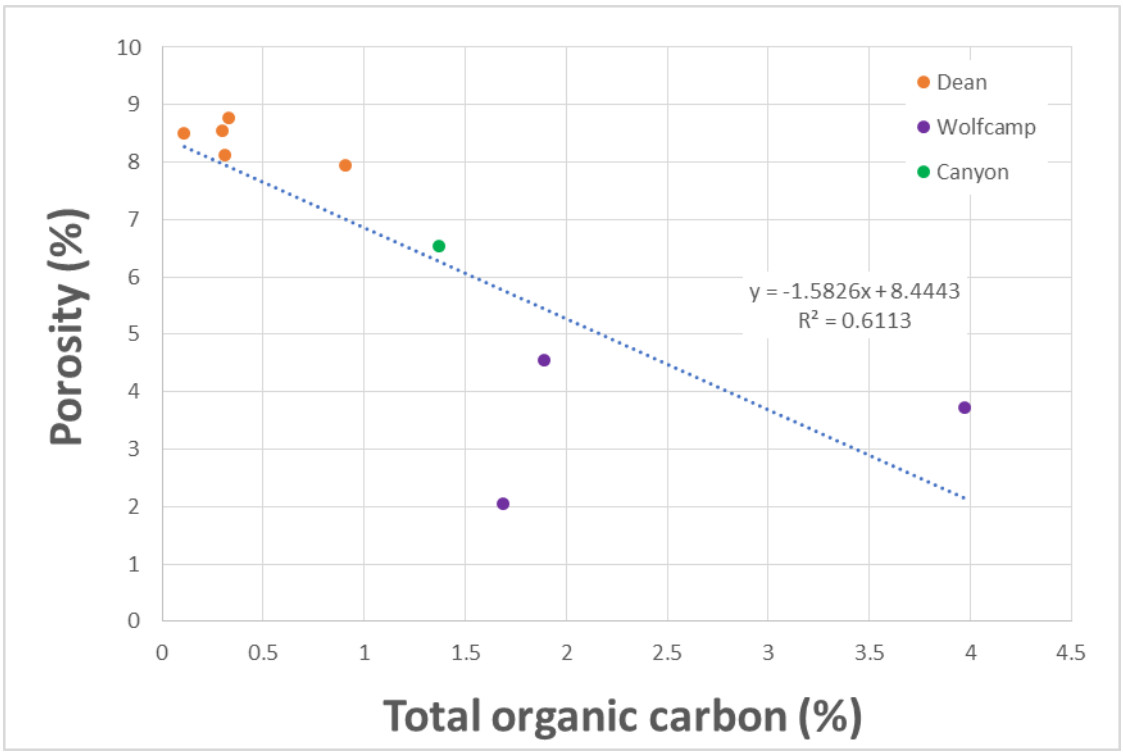

Figure 24: Porosity (MICP derived) vs. Total organic carbon

Smaller pore-throat networks are underrepresented for higher TOC samples (i.e. Wolfcamp and Canyon) compared to lower TOC samples (i.e. Dean). Table 8 shows that the median pore-throat diameter is much larger for Wolfcamp and Canyon samples relative to Dean samples. Wolfcamp samples show dominant pore-throat diameter in the 100-1110 µm range. These large pore-throat could be evidence of fluid pathways through shale laminae. It is possible that this lower pressure region is skewing results for the higher pressure (i.e. lower grain diameter) regions of MICP testing. A result of this could be that smaller pore-throat regions are not properly represented from MICP testing; which is likely when considering published MICP testing for Wolfcamp cores. Zhao et al. (2017) show Wolfcamp samples with pore diameters ranging from 2-300 nm (Figure 25). Shen and Sheng (2016) show pore-throat

diameters of Wolfcamp cores mostly lie in the range of 3-50 nm, with few between 1-10 µm. It is possible that samples tested in this study have higher degree of lamination compared to the aforementioned studies, which would allow for mercury to flow through these "sheets" more easily.

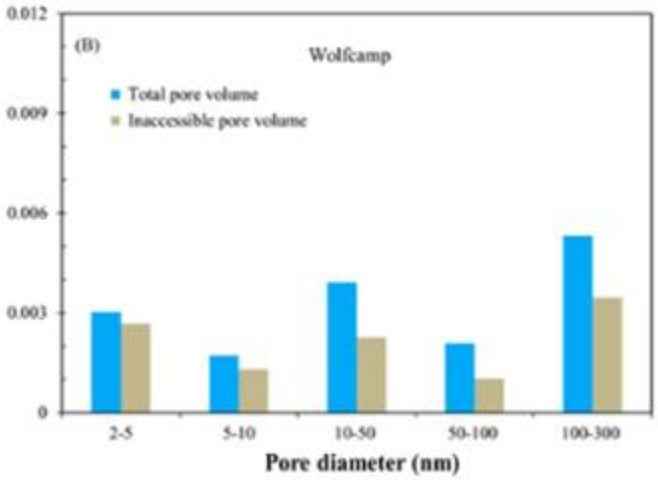

Figure 25: Plot of total and inaccessible pore volume vs. pore diameter for Wolfcamp core sample using SANS and low-pressure N_2 adsorption (Zhao et al., 2017)

Regardless of the accuracy of the smaller pore-throat region distributions for the Wolfcamp and Canyon samples, MICP data shows existence of high permeability (Darcy scale) laminae fluid pathways in the Wolfcamp and Canyon samples. It is possible that the prolific nature of hydrocarbon production in the Wolfcamp is in part due to these high permeability zones. Using helium porosimetry and nuclear magnetic resonance, Ramiro-Ramirex et al. (2018) showed high permeability (micro-Darcy scale) laminated mudstone lithofacies in the Wolfcamp formation act as preferential flow pathways during production.

When processing MICP data, samples that exhibited high permeability fluid pathways related to laminae were analyzed by separating the data into two distinct regions: “matrix” region (<50 µm) and “fracture” region (>50 µm). Porosity was calculated for each of these regions. Fracture porosity was plotted versus clay content in Figure 26. For samples that exhibit large volume of fracture porosity, there is a positive relationship between clay content and fracture sized porosity; this is likely related to the expandability of clay components in these samples.

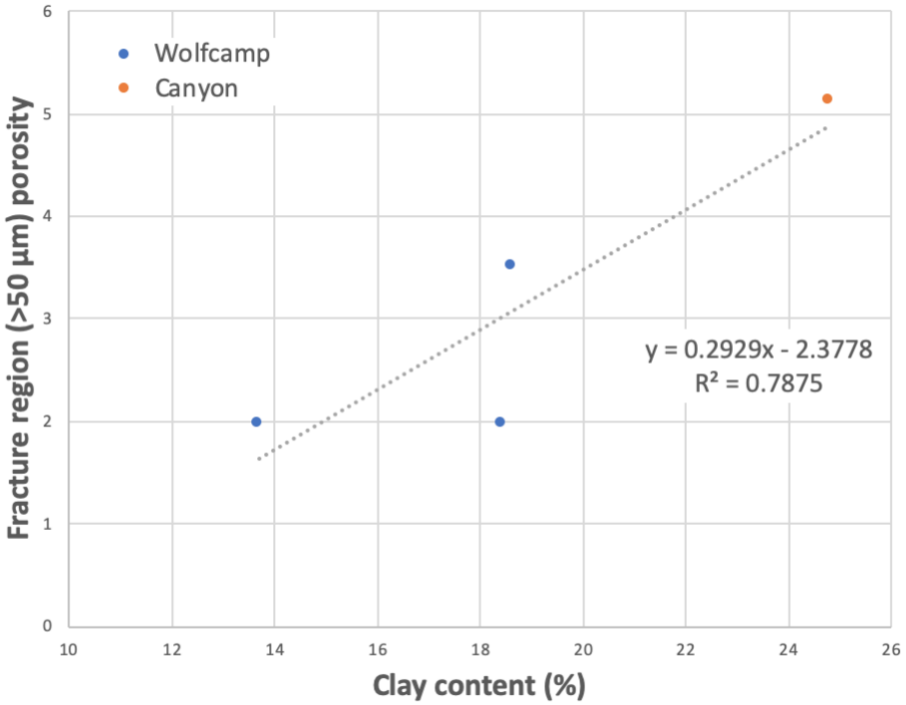

Figure 26: Fracture region (>50 µm) porosity vs. clay content. Fracture region porosity potentially related to sheet-like pore space associated with shale laminae

Samples W-8291-D and W-8291-D, silica-dominated dominated siltstones, exhibit the highest porosity of the samples tested. These two samples attribute approximately 60% of their

pore-throat diameter distribution (Table 9) to 0.1-1 μm. Reed and Loucks (2015) note that that interparticle porosity is commonly less than 1 μm and prominent in pore networks where organic material is limited. It is possible that these samples are best characterized by an interparticle pore-throat network. Dean samples W-8203-D, W-8279-D, and W-8280 are similar in mineralogy to W-8291-D and W-8292-D. The former three samples have more clay and less quartz and feldspar than the latter two. These three samples with higher clay content exhibit a dominant pore-throat diameter of 0.01-0.05 μm. This porosity diameter range is typically associated with intraparticle pore space. It is possible that this pore-throat system arose from the dissolution of clay.

Figure 19 shows high inflection points in high pressure regions (45,000-60000 psi) for samples W-8203-D, W-8279-D, and W-8280. These intrusion pressures correspond to 2.8-4 nm pore sizes by the Washburn equation. The Dean samples with only ~10 wt% clay content do not show inflection points in this pressure range. It is possible that the pore space detected between 2.8-4 nm is associated with clay-bound water. Clay-bound water arises as a result of the negative surface charge density of clays. Dipolar water molecules are attracted by clay minerals, and create a thin, immobile film of water known as the Stern layer. Stacked clay sheets could create intraparticle pore space associated with the Stern layer which could range from ~1 nm in diameter to a few nanometers (Torres-Verdin, 2016). Identification of this clay-bound is important because despite being pore space, it does not contribute to effective porosity. Samples ME-8444-WC, ME-8463-WC, and JB-10570-C show high inflection points in the interparticle clay range. ME-8455-WC and JB-9904-WC do not exhibit high inflection points at this pore diameter range. Clay content is 13.7 wt% for ME-8455-WC. ME-8444-WC, ME-8463-

WC, and JB-10570-C each have clay contents above 18 wt%. XRD analysis was not performed on JB-9904-WC. It appears that MICP inflection points are more likely to occur at 45,000-60000 psi for samples with higher clay content.

Wettability and pore connectivity

Shales unique dual-pore connectivity network is evidenced by the impact of fluid wettability on vacuum saturation, liquid pycnometry, and spontaneous imbibition. Findings from these tests suggest that Wolfcamp, Canyon, and Dean samples contain both water-wet and oil-wet pore-throats. Generally, mineralogical pore-throats are typically larger and less connected than organic pore-throats (Reed and Loucks, 2015).

Fluid imbibition results provide insight into the connectivity of this pore network. Table 14 shows distinct differences between the pore connectivity of hydrophilic fluids and hydrophobic fluids. All samples show a higher degree of pore connectivity for DT2, a hydrophobic fluid. DT2 imbibition tests show connectivity slopes near the classical diffusion value 0.5. DIW pore connectivity slopes for each sample display anomalous diffusion, ~0.25. This variation is evidence that these samples have wettability-dependent connectivity.

Pore connectivity determined from fluid imbibition shows consistency with contact angle results. Except for ME-8444-WC, each sample that was tested with contact angle tests show API brine as the most non-wetting fluid. Fluid contact tests performed with n-decane, a hydrophilic fluid, each exhibit a strong wettability to n-decane except for sample ME-8444-WC. For sample ME-8444-WC, the contact angle measurement for DIW and n-decane are 39.1° and 65.2-58.3°, respectively. This sample exhibits a relatively high DIW connectivity slope, but still in

the range of anomalous diffusivity. In discord with high DT2 contact angle measurements, DT2 connectivity slope and early imbibition rates for sample ME-8444-WC are high. It is possible that this sample has a relatively high volume of water-wet pore space while still maintaining a dominant oil-wet pore space.

Sample W-8280-D is unique in that it shows relatively high connectivity slopes for both hydrophilic and hydrophobic fluids. Contact angle tests (Figure 22) suggests this sample is wetting to both DIW and n-decane. MICP data indicates that the pore-throat diameter distribution of sample W-8280-D is 55.6% 2.8-50 nm and 37.4% >100 nm. The dominant pore type is from 0.1-0.5 µm, which is most commonly associated with intraparticle porosity. High hydrophilic pore connectivity suggest that a well-connected pore network exists that is wetting to water. It is possible that intraparticle mineral pores are water-wetting. However, Bohacs et al. (2012) note that intraparticle porosity associated with mineral grains generally does not exist in a connected network. It is unlikely the dominant pore system for this sample. Instead, it could be dominated by water-wet interparticle mineral pores. 0.1-0.5 µm pore-throat diameter, however, is small for this type of porosity.

Theoretically, porosity calculated using vacuum saturation liquid displacement should be lower than the porosity determined using MICP if the sample houses dual-wettability pore networks. For example, the pore volume penetrated by a hydrophilic fluid, DIW, would underrepresent hydrophobic pores. The porosity calculated using DIW vacuum saturation in this instance would be lower than the true porosity, as DIW might fail to penetrate hydrophobic pores. If such a pore system did not exist (i.e. uniform wettability existed across the entire pore network), then either a hydrophilic or hydrophobic fluid would penetrate the entirety of the

sample, saturating all of the pore space of the sample. In this case, vacuum saturation porosity would reflect the entire edge-accessible pore space and would be approximately equal to MICP-derived porosity, which is not affected by pore spaces of differing wettability. Vacuum saturation liquid displacement is useful because it not only provides edge-accessible porosity, but also because of this insight into wettability. Porosity results from MICP and vacuum saturation are compared in Table 16.

Sample ID	MICP	Vacuum Saturation		
		DIW	DT2	THF
W-8203-D	7.95	7.36	8.16	8.50
W-8279-D	8.12	11.21	8.81	7.41
W-8280-D	8.55	9.65	9.60	8.57
W-8291-D	8.51	10.40	9.09	7.00
W-8292-D	8.78	9.60	8.36	7.16
ME-8444-WC	3.73	0.90	2.06	0.79
ME-8455-WC	2.05	0.85	1.67	0.40
ME-8463-WC	4.56	1.49	2.11	1.34
JB-9904-WC	1.69	3.03	1.19	0.03
JB-10570-C	6.54	2.67	2.20	2.55

Table 16: Compilation of porosity (%) determined for each sample with different methods, with cubic samples.

Porosity values are somewhat consistent across each method. Generally, THF vacuum saturation porosity values are the lowest. Because THF has neutral wettability, it could fail to reach small pore spaces that would otherwise be occupied by a wetting fluid. Additionally, THF has a very high evaporation rate. The evaporation of THF when recording saturated sample weights could result in an artificially low fluid weight. This would cause the calculated porosity to be low. Comparison of porosity values calculated using DIW and DT2 provides an indication

of the dominant wetting state in the pore space. The Dean samples all have higher DIW porosity than DT2 porosity except W-8203-D. Sample W-8203-D has the highest TOC of the Dean samples, and therefore likely the highest oil-wet, organic porosity. With higher pore accessible to DT2, the calculated porosity would be higher. Three of the four Wolfcamp samples have higher DT2 porosity compared to DIW porosity, indicating a more oil-wet pore-throat system.

Bulk density values determined for granular samples using liquid pycnometry are compared to bulk density values determined for slab and cube samples in Table 9. In liquid pycnometry for granular samples, when more edge-accessible porosity was penetrated, less fluid was displaced. Because of this, a lower bulk density and higher porosity is expected for samples which have higher amount of pore space accessible to the fluid. By using DIW, DT2 and THF, a relative comparison of effective porosity can be made for different sizes of each sample. This effective porosity is related to wettability and connectivity. DIW is expected to have the highest apparent bulk density of the three fluids for dominantly oil-wet samples. This is due to more fluid being displaced because of limited connectivity to oil-wet pores. Figure 22 shows that this is the general trend for all samples tested.

The presence of edge-accessible isolated porosity is detectable by a decrease in apparent bulk density across sample size designations. Samples were tested for various sample sizes (e.g. ~4 cm slab, 1 cm^3 cube, Size GRI grains) in an attempt to vary the proportion of edge-accessible porosity to total porosity. As sample size goes down, the ratio of sample volume in contact with the sample edge goes up. As more of the sample mass is subject to the reach of edge-accessible porosity, apparent bulk density will decrease. It was expected to see this trend

manifested in apparent bulk densities decreasing with decreasing sample size. However, no such trend was established.

CONCLUSION

The existence of dual-wettability in shale across the worlds has been noted (e.g., Passey et al., 2010; Yang et al., 2017). A recognition of the importance of this phenomenon has given rise to innovative nano-petrophysical laboratory methods.

Spontaneous imbibition tests suggest that fluid flow through matrix porosity is characterized by diffusivity (driven by a concentration gradient) in the tested samples. Oil-wet, well connected organic pores dominate fluid flow through the Dean, Wolfcamp, and Canyon rock matrix. Water-wet pore-throats associated with inorganic mineral grains are less connected and characterized by slower, spontaneous diffusion.

Mercury injection capillary pressure tests suggest the presence of highly permeable flow pathways via laminae that are possibly related to clay content and lithofacies. In the Wolfcamp, mudstone lithofacies appear to act as a natural conduit to hydraulically-induced fractures, evidenced by mercury injection capillary pressure permeability from this research and helium porosimetry and nuclear magnetic resonance from Ramiro-Ramirex et al. (2018). Given the high permeability and TOC associated with this lithofacies, it could be an ideal candidate for hydrocarbon exploration.

Low connectivity in shale rock matrix is likely partially a result of edge-accessible porosity, which is investigated using vacuum saturation and liquid pycnometry. Using hydrophilic, hydrophobic, and intermediate wetting (i.e., DIW, DT2, and THF, respectively) the

porosity accessible to the sample edge is shown to have dual- wetting behavior. Hu et al. (2017) combined vacuum saturation with nanoparticle tracers to map the edge-accessible pore system. Their research showed pore-space was lower with increased distance from sample edge in the Longmaxi formation.

Quantification of pore volume accessible by hydrophyllic and hydrophobic pore space is suggested in the Wolfcamp formation for further research. Improved completion efficiency might result from a better understanding of how both injected fluid and produced fluid migrate through the rock matrix to the fracture edge.

References

American Petroleum Institute, 1998. RP-40 Recommended practices for core analysis section. API Recommend Practice, 2, Washington, D.C.: API Publishing Services.

Anders, M. H., Laubach, S. E., and Scholz, C.H., 2014. Microfractures: A review: Journal of Structural Geology, v. 69, p. 377–394, doi:10.1016/j.jsg.2014.05.011

Cloud, P.E., Jr., and Barnes, V.E., 1948. The Ellenburger Group of central Texas: Austin, University of Texas at Austin Pulication no. 4421.

Loucks, R., Reed, R., Ruppel, S., Ursula, S., Ursula, H, 2012. Spectrum of pore types and networks in mudrocks and a descriptive classification for matrix related pores. AAPG Bulletin. 96. 1071-1098. 10.1306/08171111061.

EIA (Energy Information Administration), 2018. Permian Basin Wolfcamp Shale Play Geology Review. https://www.eia.gov/maps/pdf/PermianBasin_Wolfcamp_EIAReport_Oct2018.pdf (accessed on September 15, 2019).

EIA (Energy Information Administration), 2019. Drilling productivity report for key tight oil and shale gas regions.
https://www.eia.gov/petroleum/drilling/pdf/dpr-full.pdf (accessed on September 15, 2019).

Ewing, R.P., and Horton, R., 2002. Diffusion in sparsely connected pore spaces: Temporal and spatial scaling. *Water Resour. Res.,* 38 (12), pp. 1285.

Fishman, N., Guthrie, J., and Honarpour, M., 2013. The stratigraphic distribution of hydrocarbon storage and its effect on producible hydrocarbons in the Eagle Ford Formation, South Texas: Unconventional Resources Technology Conference, Denver, Colorado, August 12–14, 2013, SPE Paper 168743, 6 p., doi:10.1190/urtec2013-157.

Flint, A.L and Flint, L.E., 2002. Particle density, laboratory methods, methods of soil analysis, Part (4), Physical methods, 3rd Edition. SSA Book Series 5. SSSA Inc, Madison, WI, pp. 229-240.

Frenzel, H.N., Bloomer, R.R., Cline, R.B., Cys, J.M., Galley, J.E., Gibson, W.R., Hills, J.M., King, W.E., Seager, W.R., Kottlowski, F.E., Thompson III, S., Luff, G.C., Pearson, B.T., Van Siclen, D.C., 1988. The Permian Basin region, Sedimentary Cover—North American Craton, L. L. Sloss, pp. 261-306.

Gao, Z. and Hu, Q.H., 2012. Using spontaneous water imbibition to measure the effective permeability of building materials. Special Topics and Reviews in Porous Media – An International Journal, 3 (3), pp. 209-213.

Gao, Z. and Q.H. Hu, 2013. Estimating permeability using median pore-throat radius obtained from mercury intrusion porosimetry. Journal of Geophysics and Engineering. 10. 025014. 10.1088/1742-2132/10/2/025014.

Giesche, H. 2006. Mercury Porosimetry: A General (Practical) Overview: Particle & Particle Systems Characterization, 23 (1), pp. 9-19.

Hager, J., 1998. Steam Drying of Porous Media. Ph.D. Thesis, Department of Chemical Engineering, Lund University, Sweden.

Handford, C.R., 1981. Sedimentology and genetic stratigraphy of Dean and Spraberry Formations (Permian), Midland Basin, Texas: American Association of Petroleum Geologists Bulletin, v. 65, no. 9, pp 1602-1616.

Hu, Q.H., Persoff, P., and Wang, J.S.Y., 2001. Laboratory measurement of water imbibition into low-permeability welded tuff. Journal of Hydrology, 242(1-2), pp. 64-78.

Hu, Q.H, 2010. UT Arlington Hydrology, Lecture Notes: Diffusion.

Hu, Q.H., Ewing, R.P., and Dultz, S., 2012. Low pore connectivity in natural rock, *Journal of Contaminant Hydrology*, 128, pp. 76-83.

Hu, Q. H., Liu, H., Zhang, Y.X., Kibria, G., Sahi, S., Altrash, N., MacDonnell, F.M., and Chen, W., 2017. Applying molecular and nanoparticle tracers to study wettability and connectivity of Longmaxi Formation in Southern China. Journal of Nanoscience and Nanotechnology 17.9, pp 6284-6295.

Katz, A. J. and Thompson, A.H., 1987. Prediction of rock electrical conductivity from mercury injection measurements, J. Geophys. Res., 92(B1), 599–607.

Miall, A., 2008. The Southern Midcontinent, Permian Basin, and Ouachitas, Sedimentary Basins of the World. 5, pp 297-327. 10.1016/S1874-5997(08)00008-7.

Oriel, S. S., Myers, A.D., Crosby, E., 1967. West Texas Permian basin region, in McKeeand, E. and Oriel, S., eds., Paleotectonic investigations of the Permian system in United States, U.S. Geological Survey Professional Paper 515-A, p. 21-64.

Passey, Q. R., Bohacs, K., Esch, W. L., Klimentidis, R., & Sinha, S., 2010. From Oil-Prone Source Rock to Gas-Producing Shale Reservoir - Geologic and Petrophysical Characterization of Unconventional Shale Gas Reservoirs. Society of Petroleum Engineers. doi:10.2118/131350-MS

Pioneer Natural Resources, 2014. The Wolfcamp Shale Technical Learnings to Date and Challenges Going Forward.

Ramiro-Ramirez, S., Bhandari, A., Reed, R., Flemings, P., and Polito, P., 2018. Porosity and Permeability in Wolfcamp Lithofacies at Delaware Basin, West Texas.

Reed, R., Loucks, R.G., 2015. Low-thermal-maturity (<0.7% VR) mudrock pore systems: Mississipian Barnett shale, southern Fort Worth basin. GCAGS J. 4, 15e28, 2015.

Rezaee M. R., Jafari, A. and Kazemzadeh E., 2006. Relationships between permeability, porosity, and pore throat size in carbonate rocks using regression analysis and neural networks.

Pommer, M. and Milliken, K., 2015. Pore types and pore-size distributions across thermal maturity, Eagle Ford Formation, southern Texas. AAPG Bulletin. 99. 1713-1744. 10.1306/03051514151.

Schlumberger, 2014. sCore Lithofacies Classification Reveals Barnett Shale Reservoir Quality.

Shen, Z., and Sheng, J., 2016. Experimental Study of Asphaltene Aggregation during CO2 and CH4 Injection in Shale Oil Reservoirs. 10.2118/179675-MS.

Torres-Verdin, C., 2016. Integrated Geological-Petrophysical Interpretation of Well Logs, lecture notes, PGE312, The University of Texas at Austin, delivered 1 August, 2017, p. 46.

Wang, S., Javadpour, F., and Feng, Q.H., 2016. Confinement correction to mercury intrusion capillary pressure of shale nanopores. Sci. Rep. 6, 20160.

Washburn, E.W., 1921. Note on a method of determining the distribution of pore sizes in a porous material. Proceedings of the National Academy of Sciences of the United States of America, v. 7, p. 115-116.

Wickard, A., Elmore, R.D. and Gerhard H., 2016. A Diagenetic Study of the Wolfcamp Shale, Midland Basin, West Texas. 10.15530/urtec-2016-2460784

Yang, R., Hao, F., He, S., He, C., Guo, X., Yi, J., Hu, H., Zhang, S., and Hu, Q.H., 2017. Experimental investigations on the geometry and connectivity of pore space in organic-rich Wufeng and Longmaxi shales. Marine and Petroleum Geology. 84. 225-242. 10.1016/j.marpetgeo.2017.03.033.

Zhao, J., Jin, Z., Hu, Q.H., Jin, Z., Barber, T., Zhang, Y.,and Bleuel, M., 2017. Integrating SANS and fluid-invasion methods to characterize pore structure of typical American shale oil reservoirs. Scientific Reports. 7. 10.1038/s41598-017-15362-0.

Appendix A)

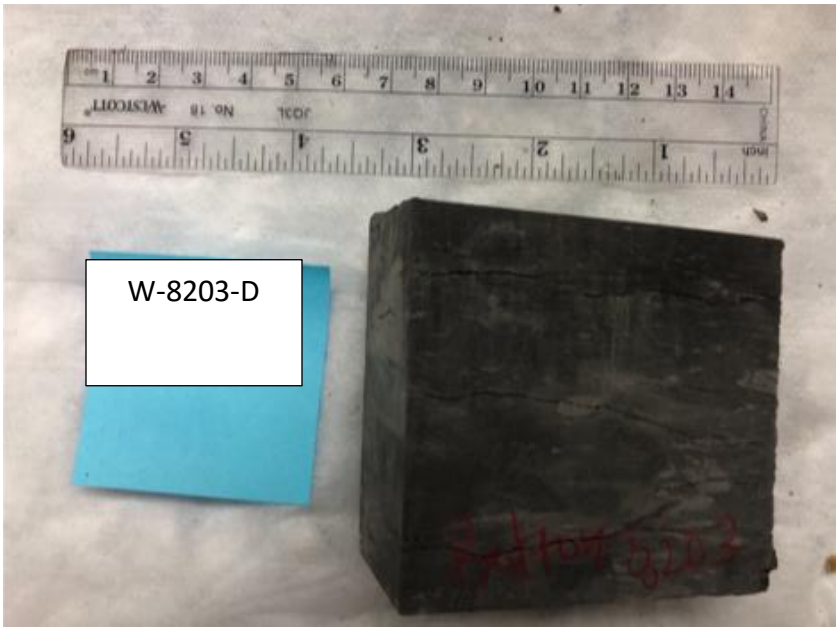


TX Dean W
8280

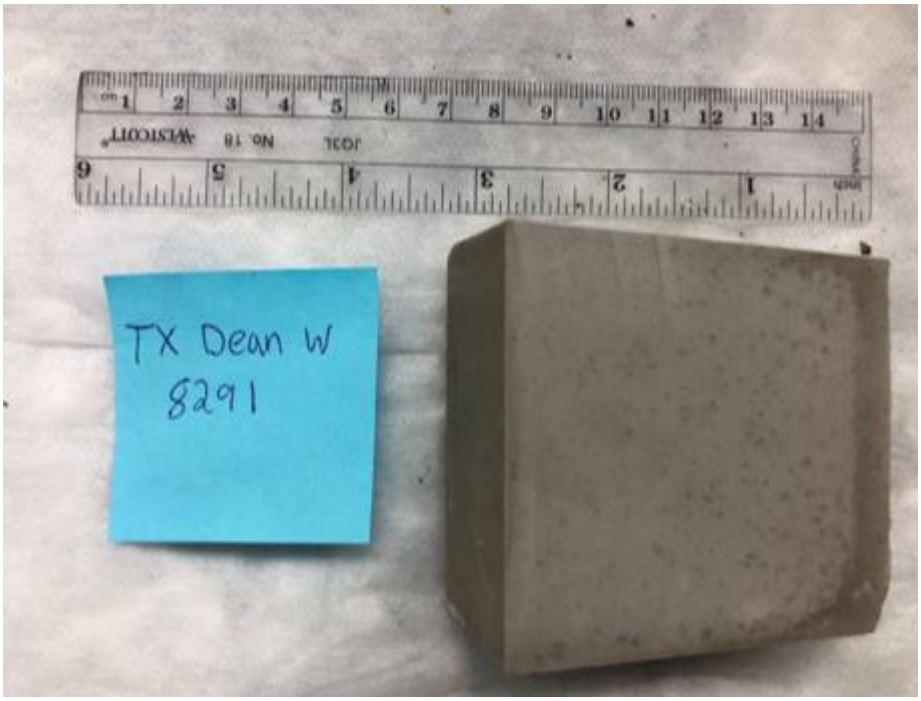
TX Dean W
8291


TX Dean W
8292


MADE IN CHINA
TX ME
8444


MADE IN CHINA
TX ME
8455


MADE IN CHINA
TX JB
9904


TX JB
10525

Appendix B)

Procedures – GeoMark Research, LLC.

1. Sample Requirements for a Typical Geochemical Program

For geochemical analysis a teaspoon (ca. 10 g.) of sample material is needed when TOC, Rock-Eval, vitrinite reflectance and residual hydrocarbon fluid fingerprinting is to be completed. If possible, a tablespoon is preferred. However, it is possible to complete a detailed program with even less sample, although there is dependency on the sample characteristics (e.g., organic richness, abundance of vitrinite, amount of staining). Sample prep includes grinding the sample with mortar and pestle until it passes through a 60 mesh sieve.

2. Total Organic Carbon (TOC) – LECO C230 instrument

Leco TOC analysis requires decarbonation of the rock sample by treatment with hydrochloric acid (HCl). This is done by treating the samples with Concentrated HCL for at least two hours. The samples are then rinsed with water and flushed through a filtration apparatus to remove the acid. The filter is then removed, placed into a LECO crucible and dried in a low temperature oven (110 C) for a minimum of 4 hours. Samples may also be weighed after this process in order to obtain a % Carbonate value based on weight loss.

The LECO C230 instrument is calibrated with standards having known carbon contents. This is completed by combustion of these standards by heating to 1200^{o}C in the presence of oxygen. Both carbon monoxide and carbon dioxide are generated and the carbon monoxide is converted to carbon dioxide by a catalyst. The carbon dioxide is measured by an IR cell. Combustion of unknowns is then completed and the response of unknowns per mass unit is compared to that of the calibration standard, thereby the TOC is determined.

Standards are analyzed as unknowns every 10 samples to check the variation and calibration of the analysis. Random and selected reruns are done to verify the data. The acceptable standard deviation for TOC is 3% variation from established value.

3. Rock Eval / HAWK Pyrolysis

Approximately 100 milligrams of washed, ground (60 mesh) whole rock sample is analyzed in the Rock-Eval or HAWK instrument. Organic rich samples are analyzed at reduced weights whenever the S2 value exceeds 40.0 mg/g or TOC exceeds 7-8%. Samples must be re-analyzed at lower weights when these values are obtained at 100 mg.

RE-II Operating Conditions

S1: 300^{o}C for 3 minutes
S2: 300^{o}C to 550^{o}C at 25^{o}C/min; hold at 550^{o}C for 1 minute
S3: trapped between 300 to 390^{o}

RE-VI Operating Conditions

S1: 300^{o}C for 3 minutes
S2: 300^{o}C to 650^{o}C at 25^{o}C/min; hold at

650°C for
0 minute
S3: measured between 300 to 400°

HAWK Operating Conditions

S1: 300°C for 3 minutes
S2: 300°C to
650°C at
25°C/min;
hold at
650°C for
0 minute
S3: measured between 300 to 400°

Measurements from Rock-Eval are:

S1: free oil content (mg HC/g rock)
S2: remaining generation potential (mg HC/g rock)
T_{max}: temperature at maximum evolution of S2 hydrocarbons (°C) S3: organic carbon dioxide yield (mg CO_2/ g rock) Several useful ratios are also utilized from Rock-Eval and TOC data. These are:

Hydrogen Index (HI): S2/TOC x 100 (in mg HC/g TOC)
Oxygen Index (OI): S3/TOC x 100
(in mg CO2/g TOC) Normalized Oil Content:
S1/TOC x 100
(in mg HC/g TOC) S2/S3:
Production Index (PI): S1/ (S1+S2)

Instrument calibration is achieved using a rock standard. Its values were determined from a calibration curve to pure hydrocarbons of varying concentrations. This standard is analyzed every 10 samples as an unknown to check the instrument calibration. If the analysis of the standard ran as an unknown does not meet specifications, those preceding data are rejected, the instrument recalibrated, and the samples analyzed again. However, normal variations in the standard are used to adjust any variation in the calibration response. The standard deviation is considered acceptable under the following guidelines:

T_{max}: ± 2°C
S1: 10% variation from established value S2: 10% variation from established value S3: 20% variation from established value

Analytical data are checked selectively and randomly. Selected and random checks are completed on approximately 10% of the samples. A standard is analyzed as an unknown every 10 samples.

4. Turnaround Time:

The standard turnaround time for sample orders over the past 12 months is approximately 2 to 3 weeks, depending on number of samples in the order.